Seismic strain and the state of stress in the crust of the Himalayas

by

Emmaline Atherton

Department of Earth Sciences, Dalhousie University, Halifax, Nova Scotia

Advisor

Djordje Grujic

Dalhousie University

Submitted in partial fulfillment of the requirements for the

Degree of Honours Bachelor of Science

Department of Earth Sciences, Dalhousie University, Halifax, Nova Scotia

Distribution License

DalSpace requires agreement to this non-exclusive distribution license before your item can appear on DalSpace.

NON-EXCLUSIVE DISTRIBUTION LICENSE

You (the author(s) or copyright owner) grant to Dalhousie University the non-exclusive right to reproduce and distribute your submission worldwide in any medium.

You agree that Dalhousie University may, without changing the content, reformat the submission for the purpose of preservation.

You also agree that Dalhousie University may keep more than one copy of this submission for purposes of security, back-up and preservation.

You agree that the submission is your original work, and that you have the right to grant the rights contained in this license. You also agree that your submission does not, to the best of your knowledge, infringe upon anyone's copyright.

If the submission contains material for which you do not hold copyright, you agree that you have obtained the unrestricted permission of the copyright owner to grant Dalhousie University the rights required by this license, and that such third-party owned material is clearly identified and acknowledged within the text or content of the submission.

If the submission is based upon work that has been sponsored or supported by an agency or organization other than Dalhousie University, you assert that you have fulfilled any right of review or other obligations required by such contract or agreement.

Dalhousie University will clearly identify your name(s) as the author(s) or owner(s) of the submission, and will not make any alteration to the content of the files that you have submitted.

If you have questions regarding this license please contact the repository manager at dalspace@dal.ca.

Grant the distribution license by signing and dating below.

_____   _____

Name of signatory   Date

Abstract

This study analyses how the seismic strain and geometry of stress in the crust of the Himalayas changes along strike of the Orogen. The active collisional setting of the Himalayas has very high rates of seismicity and thus poses a significant threat to the densely populated surrounding areas. A large-magnitude earthquake would have catastrophic effects on both the infrastructure and people of north-eastern India. Therefore, it is essential to have a good understanding of the crustal distribution of stresses in this area.

The Himalayan Orogen is characterized by a series of north-dipping thrust faults and shear zones formed as a result of the ongoing convergence of the Indian and Eurasian tectonic plates. The Main Frontal Thrust (MFT), the Main Boundary Thrust (MBT), and the Main Central Thrust (MCT) span the entire length of the Orogen and merge at depth into the Main Himalayan Thrust (MHT) – the basal detachment of the Himalaya. The majority of seismicity is concentrated along a belt located approximately 100 km north of the mountain front. In a section of the eastern Himalaya (the Bhutan Himalayan region) the seismic belt is interrupted and there have been no major seismic events in this area in written record. Since the geodetic convergence rates in the eastern Himalaya are higher than in the west, and the lithology does not change significantly, the lack of seismicity in this area is puzzling. This study uses records of crustal seismicity to determine and quantify changes in seismic strain along strike of the Orogen.

The Himalaya was separated into five geographic regions and fault-slip inversion was performed on the corresponding seismic data. Three crustal fault regimes were identified: thrust, strike slip, and normal. Events belonging to the normal fault regime are located along the southern margin of the Tibetan Plateau. From west to east, the normal faults indicate predominantly E-W extension which is interpreted to be the result of faulting along the South Tibetan Grabens. Other results show a prominent thrust fault regime in the seismic belt of the western to central Himalaya. Most of these events yield solutions compatible with thrusting along a ramp of the MHT. In contrast, a strike-slip faulting regime is dominant both in the eastern Himalaya (east of 87°E) and to the south of the Himalaya in the Shillong Plateau. The latter is the only elevated area outboard the Himalaya and is one of the most seismically active areas covered in this study. There appears to be a direct link between the seismic strain conditions that contribute to the thrust and strike slip faulting regimes; however, results show that thrust faults dominate the western regions of the Himalayas, while strike slip faults dominate the eastern regions. Calculations were performed on the seismic data to quantify the total amount of energy released on these respective fault types, as well as the total amount of slip that has occurred. The conclusion was that the increased convergence rates in the eastern Himalaya may be accounted for by the increase in strike slip faulting activity in this region of the Orogen. This result may suggest that the MHT in the eastern Himalaya is not accumulating as much seismic strain from the higher convergence rate as previously theorized; rather, the plate convergence is being released as slip along transverse faults in the Indian crust.

Key words: Himalayas, crustal seismicity, fault slip inversion, seismic energy, slip rate, seismic gap

Acknowledgements

Table of Contents

List of Figures

List of Tables

1.0 Introduction

1.1 General Statement

The on-going collision between the Indian and Eurasian tectonic plates has created a structurally complex plate boundary with high rates of seismicity. In certain areas along the plate boundary large seismic events have the potential to be very destructive to nearby cities. Developing a thorough understanding of how stress from the northward movement of India is accommodated in the crust of the Himalaya is necessary so that cities can build infrastructure accordingly.

North-south shortening at the boundary of the Indian and Eurasian tectonic plates has led to crustal thickening that is characterized by a series of thrust faults oriented along strike of the Orogen. However, there is an area along the Orogen between eastern Nepal and Bhutan that is dominated by strike slip faults (De & Kayal, 2003; De & Kayal, 2004; Drukpa *et al.,* 2006) that spatially overlaps with an area of low seismicity in the Bhutan Himalayan region (referred to here-on as a seismic gap) (Gahalaut *et al.,* 2011) (Fig. 1.1). This strike-slip fault dominated region has not been assessed in comparison with the thrust-fault dominated areas to the east and west in terms of strain distribution and shortening. This study aims to provide an analysis of how the seismic strain varies along strike of the Orogen, as well as with depth, in hopes of adding insight into the area dominated by strike slip faults. The hypothesis of this thesis is that variations in strain geometry will be evident between eastern Nepal and Bhutan that are associated with the strike slip-dominated area, and can also help account for the lack of seismic events in the seismic gap of the Bhutan Himalayas.
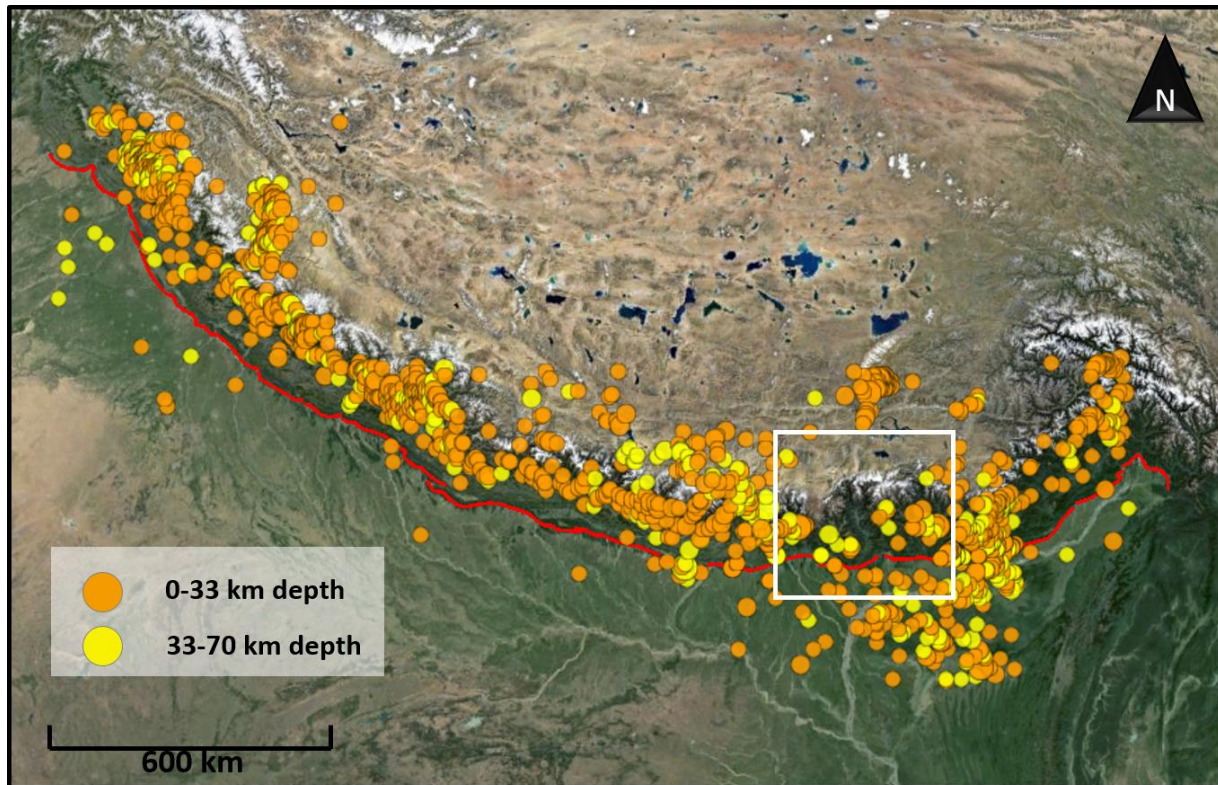
Figure 1.1: Magnitude 4 and greater earthquakes from 1977–2014 in the crust of the Himalayas obtained from the ANSS catalogue. The seismic gap is located in the Bhutan Himalayan region, north of the Shillong Plateau. Orange circles represent shallow crustal (0-33 km deep), yellow circles represent slightly deeper crustal earthquakes (33-70 km deep). (Map data: Google, Mapabc.com).

The seismic gap in the Bhutan Himalayan region is a unique area because it has experienced very few large seismic events in the historical past (Gahalaut *et al.,* 2011). Due to a lack of data before historical records, the seismic gap is recognized only as a lack of seismicity in the last ~40 years. However, seismic events are constantly taking place in the Himalayas, so although the gap is only based on recent data, it is still important to understand the causes behind it. Major- and great-scale earthquakes (magnitude 7 and higher) that have been recorded since 1900 in the Himalayas include: Kangra (1905) of M_w 7.8, Uttaranchal (1916) of M_w 7.3, Nepal-Bihar (1934) of M_w 8.1, Assam (1947) of M_w 7.3, and Assam Tibet (1950) of M_w 8.5 (Bilham & Ambraseys, 2005). Of all these large-scale earthquakes, none have occurred within the seismic gap of the Bhutan Himalaya region.

1.2 Significance

The seismic gap in the Bhutan Himalayan region suggests the risk of a major- or great-scale earthquake occurring to relieve the potential build-up of stress. It is currently estimated that there is 4 m of potential slip accumulating in the Bhutan Himalayan region, which corresponds to an earthquake of magnitude 8 or higher (Bilham *et al.,* 2001). A large-scale earthquake in this region of the Himalayas would be devastating because of the recent increase in population as well as the large population densities in these areas. A conservative estimate of over 50 million people would be affected throughout Assam, Meghalaya, Bangladesh, and Bhutan if such an event were to occur. Furthermore, the economic growth in these regions has resulted in an increase of infrastructure that has not been designed in preparation for large-scale earthquakes. Studying the changes in the geometry of stress in the crust of the Himalaya will give insight into this area of concern.

1.3 Data Compilation and Study Area

To assess the seismic strain distribution and crustal stress geometry in the Himalayas, earthquake data were compiled from the ANSS catalogue (USGS), Baruah *et al.* (2014), and also from the Global Centroid-Moment-Tensor Project (GCMT). The methods used for the GCMT catalogue are described by Dziewonski, *et al.* (n.d.) and the types of analyses used are described by Ekstrom, *et al.* (n.d.). Records are complete in these catalogues from 1977 onwards for earthquakes of magnitude 4 and higher. Prior to 1977, sufficient recording instruments were not in place to detect earthquakes in all areas of the Himalayas. Therefore, in order to eliminate any biases based on available technology we have constrained the time span of this study to 38 years. Where most of the seismicity is located in the Himalayas the crust extends to a depth of 70 km (Avouac, 2003). The seismic

data used in this study was therefore limited to depths of 10-70 km so that only seismic events in the crust were analysed.

Two software programs (Faultkin 7 (Version 7.2.9) and T-Tecto (Version 3.0)) were used to perform fault-slip inversion and conduct paleostress analysis from the seismic data. To do this, the entire Himalayan mountain range was divided into five geographic areas so that the results from the paleostress analysis could be compared along strike of the Orogen (Fig. 1.2) (Table 1.1). These areas were chosen based on where seismicity was clustered along the Himalayas, as well as the amount of available data. Hypocenter depths were also considered in order to properly assess the state of stress distribution and geometry of strain from seismic events.
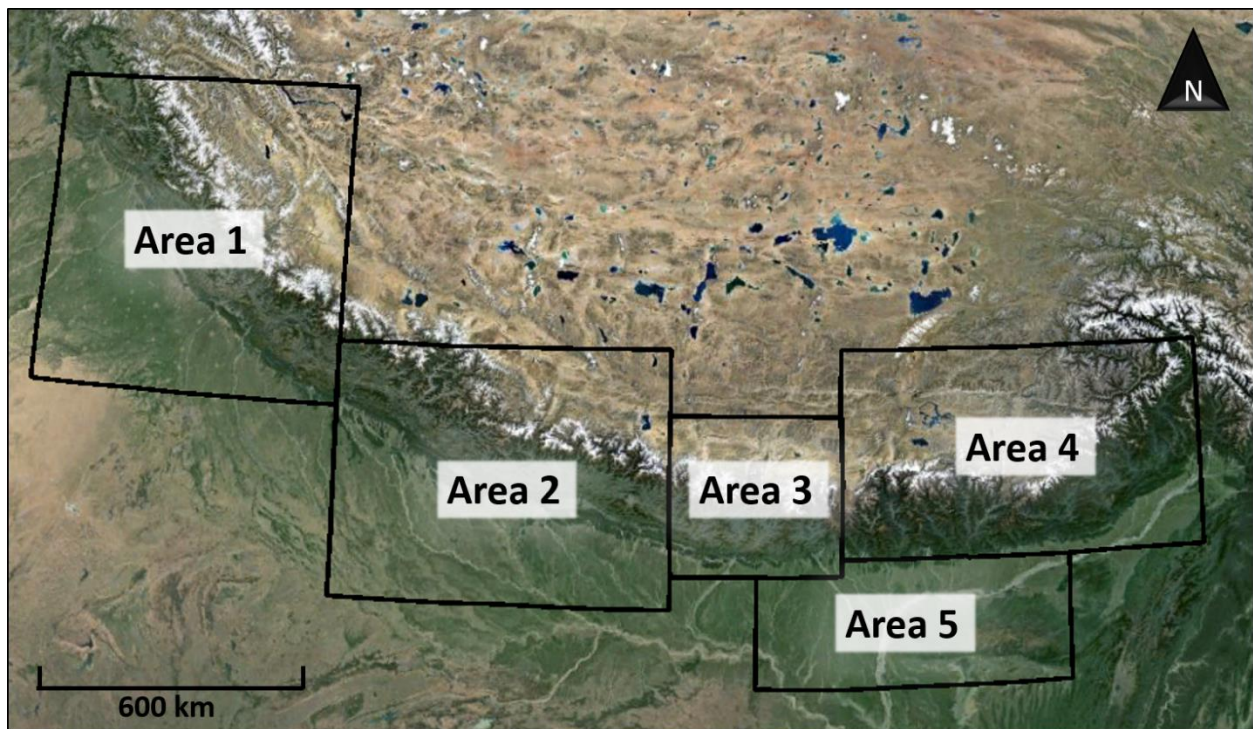
Figure 1.2: Map of the Himalayas and the geographic areas created for this study so that results could be compared from west to east along the Orogen. These areas were chosen based on clusters of seismicity, as well as the amount of available data. Area 5 is concentrated over the Shillong Plateau (a very seismically active structure outside of the Himalayan Orogen). (Map data: Google, Mapabc.com).

Table 1.1: Latitude and longitude values covered by each of the five areas outlined in Figure 1.2.

Area	Latitude	Longitude
1	29.0° N - 34.0° N	74.0° E - 80.0° E
2	26.0° N - 30.0° N	80.0° E - 86.0° E
3	26.5° N - 29.0° N	86.0° E - 89.0° E
4	26.7° N - 30.0° N	89.0° E - 95.5° E
5	24.7° N - 27.0° N	87.5° E - 93.0° E

2.0 Geological Background

2.1 Tectonic History

The Indian and Eurasian tectonic plates collided ~50 Ma (as cited in Molnar & Stock, 2009). Prior to the collision the northern margin of the Indian subcontinent was passive, and sediments were deposited in the Tethys Ocean. To the north, the southern margin of the Eurasian plate was active where the oceanic crust of the Tethys Ocean was being subducted beneath the volcanic continental crust. When India and Eurasia collided, a suture zone was formed at the plate boundary, joining the sedimentary rocks of the passive Indian margin, and the igneous and sedimentary rocks of the active Eurasian margin. This suture zone is referred to as the Indus-Yarlung Suture Zone (IYSZ) and runs the entire length of the Himalayan Orogen (Avouac, 2003).

The collisional processes that have been occurring between the Indian and Eurasian tectonic plates have created a 2500 km-long, and up to 200 km wide, mountain chain that contains the highest peaks in the world (Hodges, 2000). The continual northward movement of India has caused the Himalayas to have high rates of seismicity, making it an area of high seismic hazard with a large population density.

2.2 Key Structural Features

The Himalayan Orogen is a geographically expansive study area. The structural complexity of the region makes the geological setting complicated; however, important to this study are the dominant, structures that distinguish this active continental collision. The following is a description of the large-scale structural features of the Himalayas and surrounding area.

2.2.1 Thrust Faults

The Himalayas are characterized by a series of forward-propagating, north-dipping thrust faults that span the entire length of the Orogen (Fig 2.1). From north to south and in order of their activation these are: the Main Central Thrust (MCT), the Main Boundary Thrust (MBT), and the Main Frontal Thrust (MFT). The deformation that has occurred along these thrust faults has resulted in thickening of the Himalayan crust from 40 km in the foreland to 75-80 km beneath the southern margin of Tibet (Fig. 2.2) (Avouac, 2003). The strike of these thrust faults changes with the curvature of the mountain range from NW-SE in the western regions to E-W in the eastern regions. The MFT is the currently active structure in this series of thrust faults. The MCT, MBT, and the MFT are shallowly
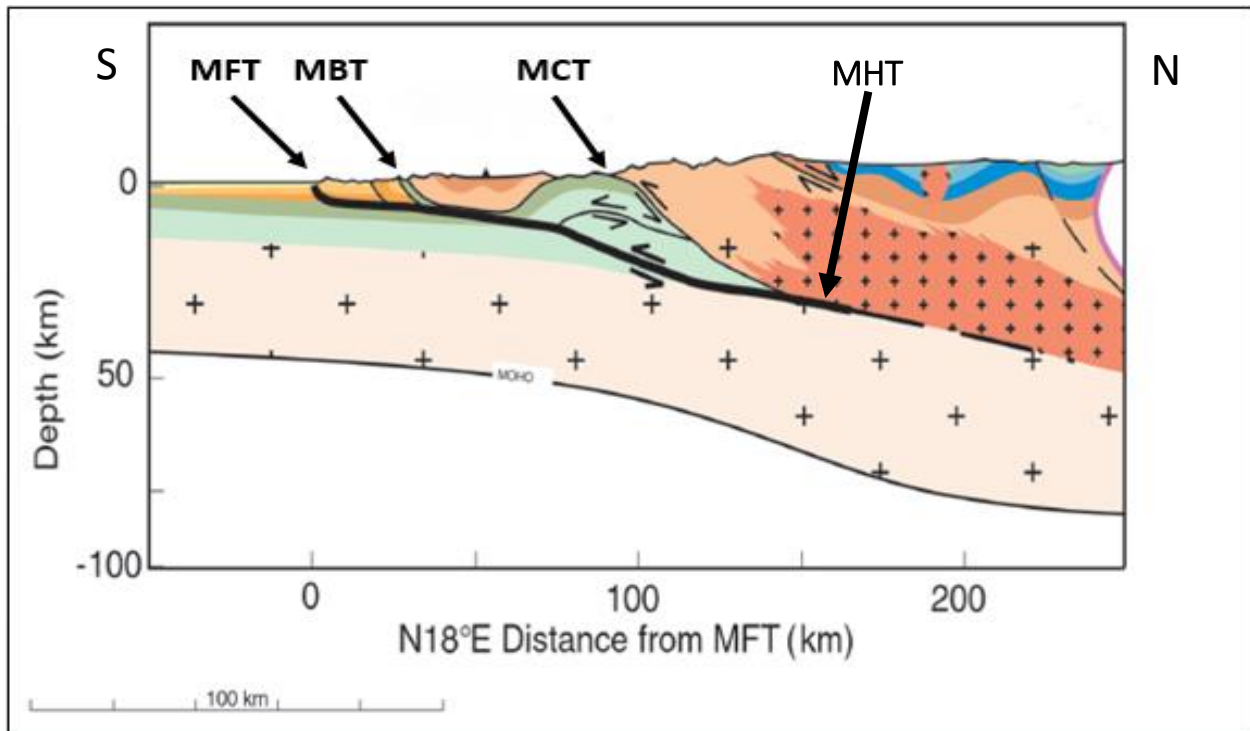
Figure 2.1: Schematic cross-section of Himalayas from central Nepal showing the main thrust faults: the Main Frontal Thrust (MFT), the Main Boundary Thrust (MBT), and the Main Central Thrust (MCT). The Main Himalayan Thrust (MHT) – the basal detachment fault of the Himalayas - is also indicated. The Indus-Yarlung Suture Zone (IYSZ) is to the north. (Modified from Avouac, 2003).

dipping northward and join at depth in the crust of the Himalaya to form the Main

Himalayan Thrust (MHT), which is the basal detachment fault of the Himalayas (Avouac,

2003).
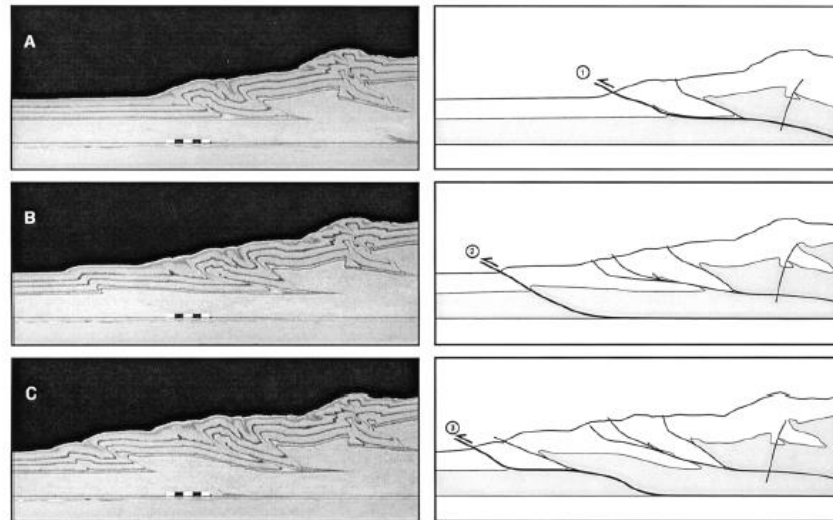
Figure 2.2: Model showing the development of the forward-propagating sequence of thrust faults in the Himalaya and the resultant thickening of the crust (Avouac, 2003). Note the bolded fault in the right images represents the most recently active thrust fault.

2.2.2 Strike Slip Faults

The majority of seismic events within the Himalayas are related to a thrust fault

regime, associated with movement along the series of shallow, northward-dipping thrust

faults. However, the Bhutan Himalayan region is dominated by strike slip faulting events,

interpreted to be caused by the oblique convergence of India and Eurasia in this area (De &,

2004; Drukpa *et al.,* 2006). The oblique convergence has resulted in transcurrent

deformation occurring at depth in the crust of the Himalaya in this region (Drukpa *et al.,*

2006). There is also evidence that this lateral motion is occurring along N-S trending right-

lateral strike slip faults (De & Kayal, 2004). This region is therefore seismotectonically

unique when compared to the thrust-fault dominated Himalayas to the east and west.

2.2.3 South Tibetan Grabens

North of the Himalayan Orogen is the Tibetan Plateau. This elevated area of low relief is characterized by multiple N-S trending normal faults that create the South Tibetan Grabens (Fig. 2.3). The orientation of these normal faults does not change with the curvature of the Orogen. These grabens are the result of E-W extension of the Tibetan Plateau (Angelier, 1984; Armijo *et al.*, 1986; Ratschbacher *et al.,* 2011; Langille *et al.,* 2014). This lateral extension and thinning of the crust of the Tibetan Plateau is interpreted to be caused by either the increasing elevation of the plateau due to convergence and plateau formation, other geodynamical processes occurring in the plateau that are unrelated to the processes of plateau formation (Blisniuk *et al*., 2001), or the change in plate convergence rate through time (Molnar & Stock, 2009).
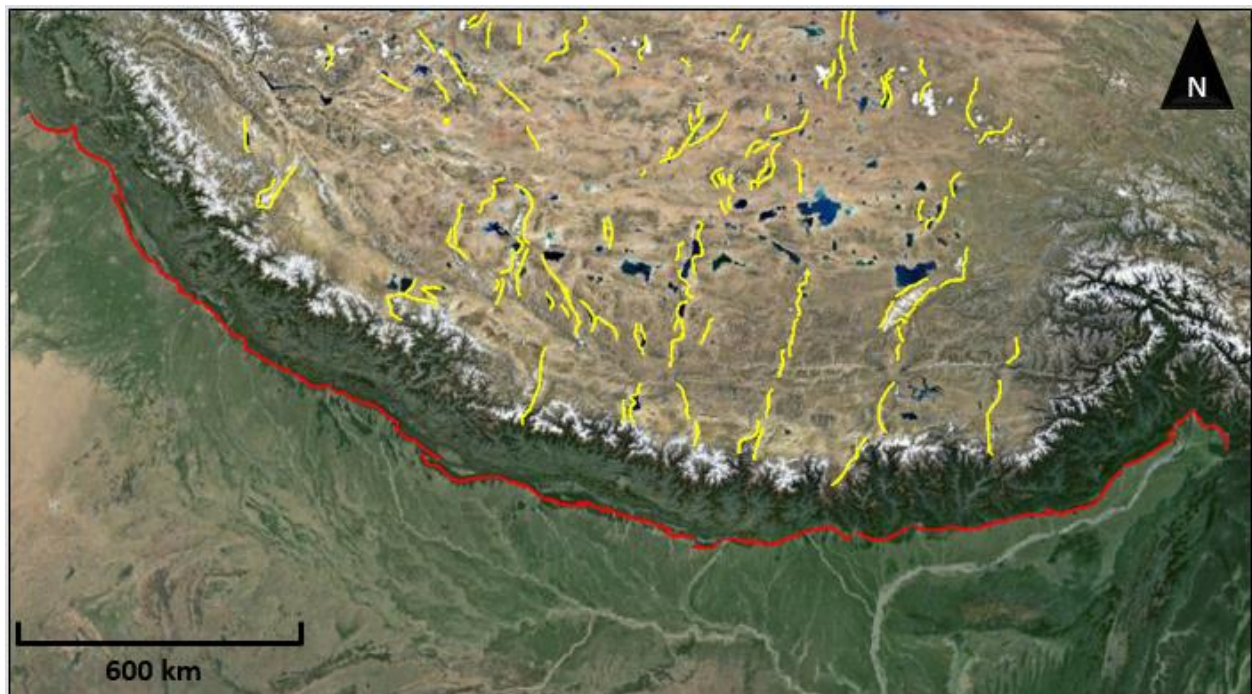
Figure 2.3: Map of the Himalayas with the South Tibetan Grabens outlined in yellow. Note that the study areas (Fig 1.2) do not include the majority of the grabens. The MFT is outlined in red for reference. (Map data: Google, Mapabc.com).

2.2.4 Shillong Plateau

Another notable structure that is associated with the eastern Himalayan range is the Shillong Plateau – the only elevated area outboard the Himalaya. Two reverse faults bound the plateau: the Oldham Fault on the northern side, and the Dauki Fault on the southern side (Figure 2.4). The collisional forces of the plate boundary between India and Eurasia, the weight of the Himalaya in the north, and of the Bengal fan sediments to the south, act as driving forces that have caused the Shillong plateau to uplift along these reverse faults, and it is therefore interpreted to be a pop-up structure (Bilham & England, 2001). Alternatively, these steep faults are interpreted to be reactivated normal faults due to Precambrian rifting, the breakup of Gondwana during the Paleozoic (Banerjee *et al.,* 2008), or during the break up of India and Australia in the Jurassic which caused the formation of the current east Indian passive margin (Biswas *et al.,* 2007). Or lastly, another tectonic model for the formation of the Shillong plateau assumes the Shillong plateau is a crustal antiform with a northward migrating fold hinge (Clark & Bilham, 2008).
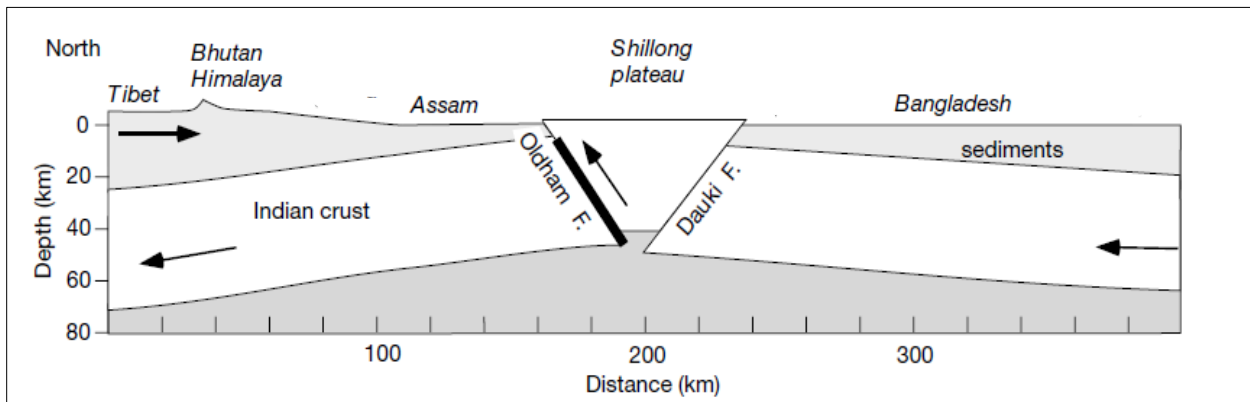
Figure 2.4: Cross-section from Tibet to the Bay of Bengal from North to South (Bilham & England, 2001). The pop-up structure of the Shillong Plateau is depicted, and is bound by two reverse faults: the Oldham fault to the north, and the Dauki fault to the south.

2.3 Rates of Indian-Eurasian Convergence

The convergence of the Indian and Eurasian tectonic plates is defined by a continental subduction zone that is dominantly driven by slab pull (Patriat & Achache, 1984). The rate of this convergence has not been consistent since the initial collision of the two continents ~50 Ma (as cited in Molnar & Stock, 2009). For the purpose of this study, only geologically recent convergence rates are important. From 10 Ma until present, Molnar and Stock (2009) propose relatively steady convergence rates of 34 mm/year for the north-western corner, and 44 mm/year for the north-eastern corner. The difference in plate velocities from the northwest to the northeast corners of the Indian plate is associated with plate rotation.

Since the Indian plate initially contacted the Eurasian plate, India has undergone counter-clockwise rotation with respect to Eurasia (Fig. 2.5) (Patriat & Achache, 1984). Contact between the northern edge of India and the southern edge of Eurasia did not occur simultaneously across the region. As the Tethys Ocean was closing, differing amounts of slab-pull occurred across the contact which affected the direction that India moved relative to Eurasia. The northwestern corner of India contacted the Eurasian plate first, and thus the convergence rate in this region slowed down in comparison to the northeast corner. Consequently, the northward movement of India has experienced a counter-clockwise rotation relative to Eurasia, and this effect was strongest during the onset of collision (Patriat & Achache, 1984).
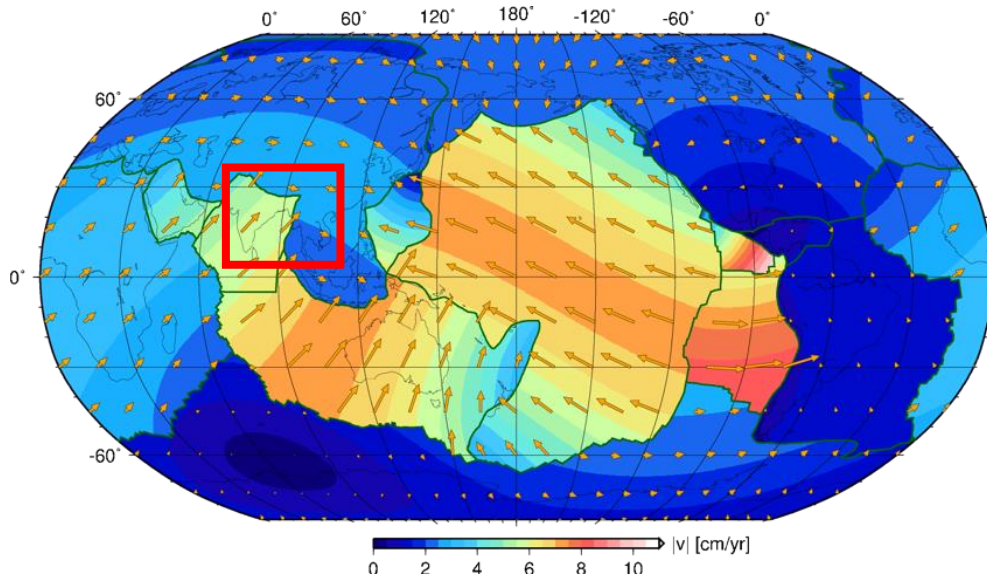
Figure 2.5: NUVEL1A velocities in the NNR reference frame (from DeMets *et al.*, 1994 after Becker). Velocity vectors show the counter-clockwise rotation of the Indian subcontinent relative to Eurasia (India in red box).

Both the increasing rates of N-S convergence towards the eastern side of the mountain range and the rotational movement of the Indian plate relative to the Eurasian plate, greatly influence how the energy from the collision is translated into contraction, or shortening, across the mountain range.

2.4 Contraction across the Himalayan Orogen

A portion of the north-south convergence of the Indian and Eurasian plates is translated into contraction across the Himalayan Orogen where deformation occurs (Zhang *et* al., 2004). The majority of this contraction is accommodated in the 10-km wide MFT zone (Burgess *et al.*, 2012). Eastward-increasing contraction rates along the Indian-Eurasian collisional zone have a similar pattern to the eastward-increasing convergence rates discussed previously. For example, the Holocene contraction rate of 23.4 ± 6.2 mm/year obtained from the eastern Himalaya compares to the 21 ± 1.5 mm/year rate in

the central Himalaya but is much larger than the contraction rate of 9 ± 3 mm/year in the

western Himalaya (Fig. 2.6) (Burgess *et al.,* and references therein 2012).
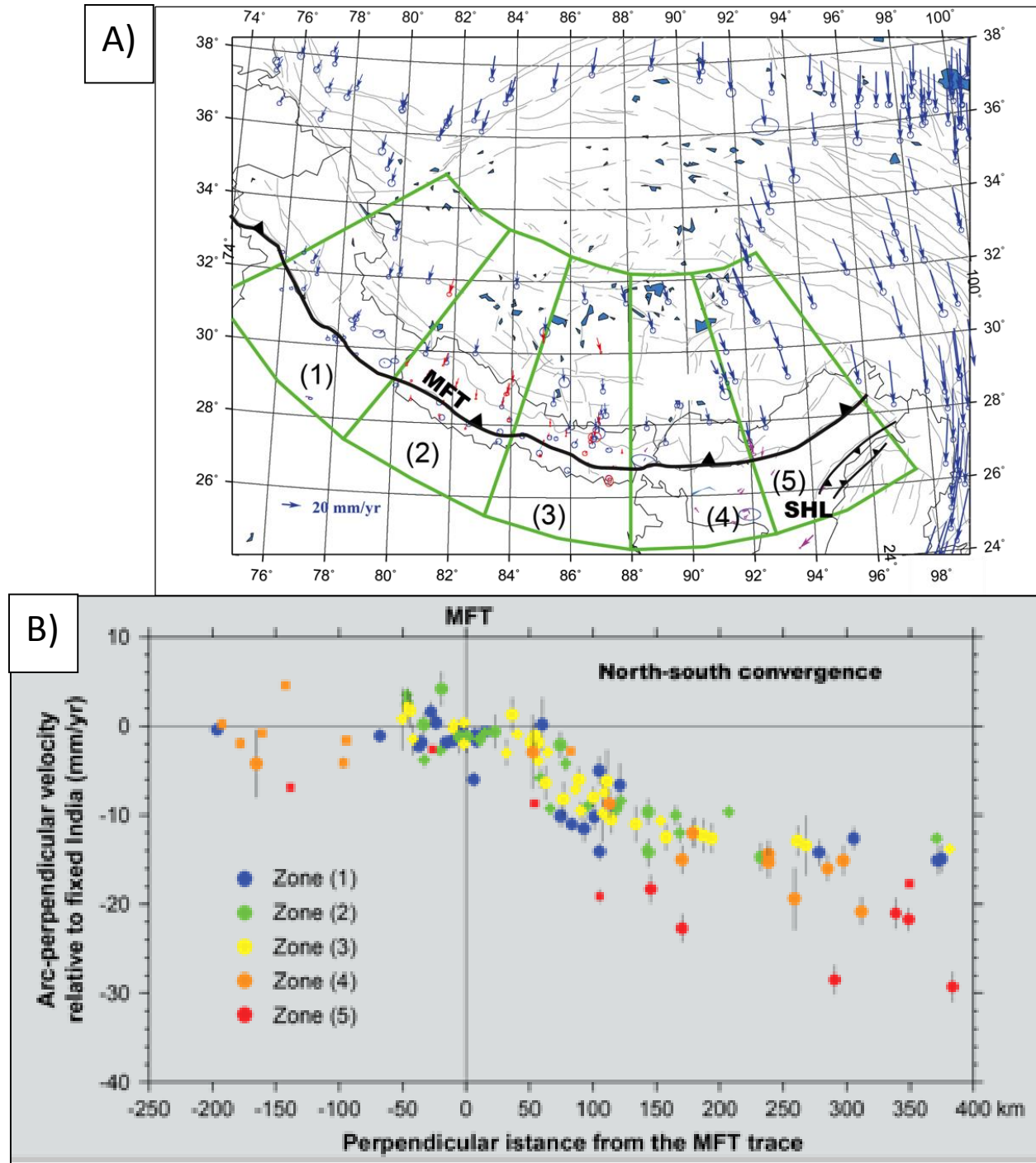
Figure 2.6: Five radial zones along the Himalayan arc where GPS measurements were taken across the MFT (A) and the corresponding contraction measurements perpendicular to the arc and relative to stable India (B). The eastern zones (4 and 5) show an increase in contraction rates of ~10 mm/year relative to the zone furthest west (zone 1) (From Burgess *et al.*, 2012).

16

Northward movement of the Indian plate into the Eurasian plate is partially accommodated by contraction across the Himalayan arc and also in the Tibetan Plateau. Increased contraction is occurring in the eastern Himalayas compared to the western Himalayas (Burgess *et al.*2012; Banerjee *et al.,* 2008) and this is closely related to the eastward increasing convergence rates (Molnar & Stock, 2009).

2.5 Seismicity

The northward convergence of India into stable Eurasia has resulted in a continental collision setting with very high rates of seismicity. The majority of this seismicity is organized into a seismic belt that runs from west to east along the Orogen and is located ~100 km north of the surface trace of the MFT (Fig. 2.7).

The Main Himalayan Thrust (MHT) has an average dip of 10 degrees to the north. It is locked for a distance of 100 km from the surface trace (the MFT), corresponding to a depth of ~15- 20 km (Ader *et al.,* 2012). Where the MHT is not locked, slip along this ramp generates the majority of Himalayan seismicity at depth contributing to the seismic belt (Cattin & Avouac, 2000; Ader *et al.*, 2012). This seismic belt is clustered into areas of high seismicity and low seismicity; however, particular attention should be paid to the seismic gap in the Bhutan Himalaya as this area has not experienced a large-magnitude earthquake in historical past (Fig. 1.1) (Gahalaut *et al.*, 2011). This lack of seismicity could be attributed to complete locking on the MHT, which would indicate an accumulation of strain due to the high rates of convergence in this area (Bilham *et al.*, 2001).

In addition to the seismic belt of the Himalayas, the Shillong Plateau also experiences high rates of seismicity (Fig. 2.8). The proximity of this tectonically-active feature to the seismic gap in the Bhutan Himalayan region makes it significant to this study.

The great Assam earthquake of 1897 was the largest to have occurred in this region in

historical records. It occurred on the northern bounding fault of this pop-up structure (the

Oldham fault) and has been theorized to have created a stress shadow causing the lack of

seismicity in the Bhutan Himalaya (Bilham & England, 2001; Banerjee *et al.*, 2008; Gahalaut

et al., 2011).
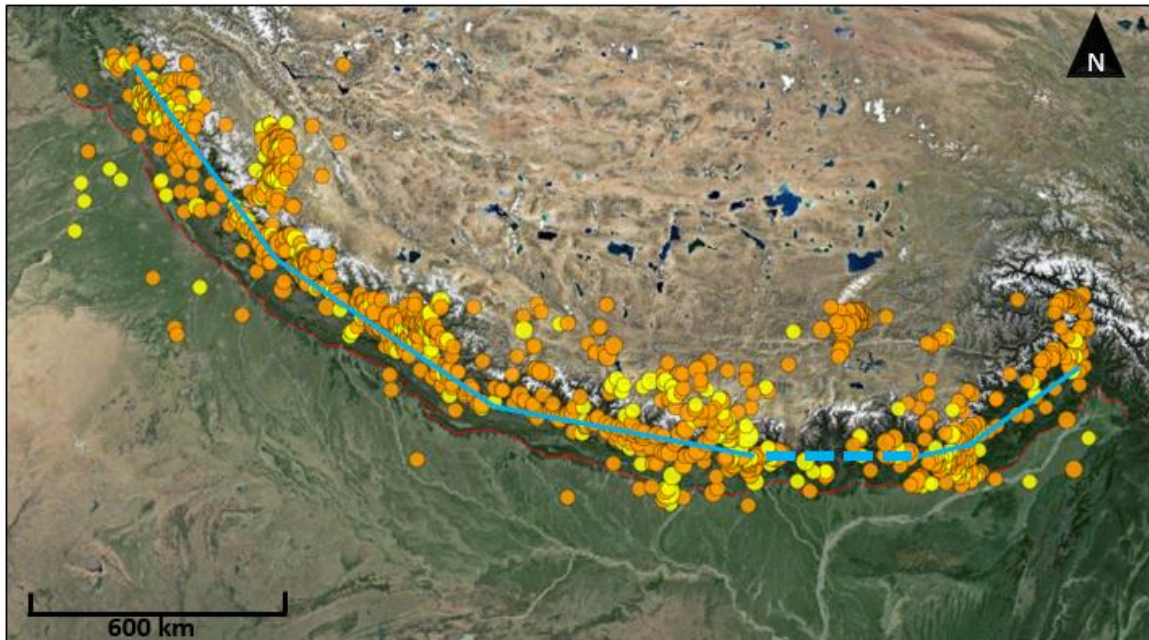
Figure 2.7: The seismic belt of the Himalayas based on epicenters of seismic events
from 1977-2014 from the ANSS catalogue. The seismic belt (blue line) is located
~100 km north of the surface trace of the MFT (thin, red line). The seismic gap is
indicated by the bolded, dashed blue line. Orange circles represent shallow crustal
earthquakes (0-33 km deep), yellow circles represent slightly deeper crustal
earthquakes (33-70 km deep). (Map data: Google, Mapabc.com).
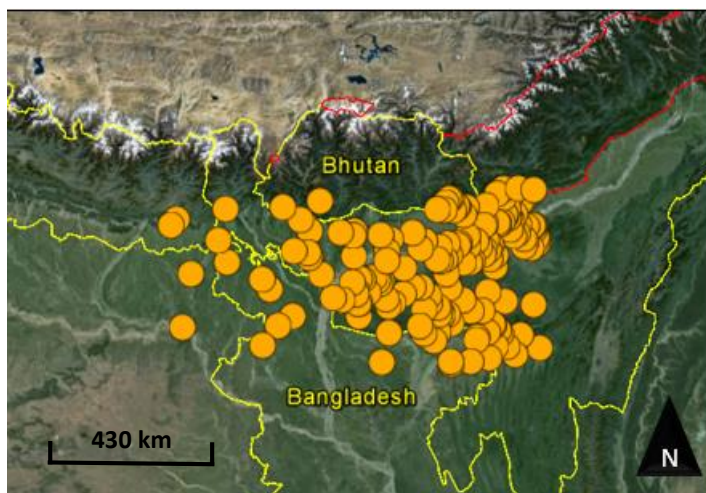
Figure 2.8: Epicenters of
seismic events in the
Shillong Plateau region
from 1977-2014. Data from
the ANSS catalogue. (Map
data: Google, Mapabc.com).

3.0 Methods

3.1 Data and Software Used

To complete this study, fault slip inversion and kinematic analysis was performed on seismic data from five pre-defined geographical regions along the Himalayan arc (Fig. 1.2). To analyse the state of stress in the crust of the Himalayas, the seismic data were input into two computer programs: Faultkin 7 (Version 7.2.9) and T-Tecto (Version 3.0). Faultkin is based on algorithms that are described by Marret and Allmendinger (1990) and Allmendinger *et al.* (2012). Both of these programs were used to plot and calculate various seismic properties on stereographic projections. Additionally, T-Tecto was used to create Mohr diagrams.

The seismic data used in this study were obtained from the ANSS catalogue (U.S. Geological Survey), the Global Centroid-Moment-Tensor catalogue (GCMT) and from Baruah *et al.* (2013) (Appendix A). The properties of the seismic data that were used in this study include: the latitude and longitude of the epicenters, the depth of the hypocenters, the orientations of the nodal planes, the seismic moment (M_o), and the magnitudes of the seismic events (the body-wave magnitude (m_b), the surface-wave magnitude (M_s), and the moment magnitude (M_w)).

The lithologies along the plate boundary between India and Eurasia are relatively consistent along the Indus-Yarlung Suture Zone (IYSZ). Because this study compares the crustal stress regimes along strike of the Orogen there are no significant changes in lithology that affect the analyses performed.

19

3.2 Terms and Concepts

In order to thoroughly explain the types of analyses that were implemented in this study (such as fault slip inversion and kinematic analysis), it is helpful to first provide a list of definitions of seismotectonics terms that will be referred to here-on (Table 3.1).

Table 3.1: Definitions of seismotectonic terms and concepts referred to throughout the following chapters (Fossen, 2010).

Stress	A measurement of the force per unit area acting on a body of rock. The stress ellipsoid is a geometric representation of the stresses acting on a point, and can help simplify these forces into three principal stresses.
Principal stresses	When combined, they create the stress ellipsoid for a region, which is an imaginary deformed sphere that provides information on the state of stress at a particular point in a rock. They are defined as σ_1, σ_2, and σ_3 from maximum to minimum stress respectively.
Normal stress	The component of stress that is perpendicular to the fault surface.
Shear stress	The component of stress that is parallel to the fault surface.
P- and T-Axes	The orientations of the compressive (P-) and tensile (T-) axes are constrained by plotting the first arrivals from seismological observatories. The orientations of the first arrivals varies based on the type of movement that occurs on the fault.
P- and T-Sectors	The majority of P-axes plot in the P-sector and the majority of T-axes plot in the T-sector. They are defined on the focal mechanism as quadrants that are separated by the nodal planes.
Nodal planes	Determined by measuring the P- and S- waves that radiate from the earthquake hypocenter. On a stereographic projection they separate the P- and T-axes. One of these planes represents the fault plane, which is the plane along which the slip occurred, while the other plane is the auxiliary plane, which is complementary and orthogonal to the fault plane.
Focal Mechanism	A stereographic projection of the first motion that occurred on a fault during a seismic event. It is created by plotting the orientations of the P- and T- axes from multiple seismograms and finding the resultant nodal planes. It provides

	information about the type of movement that occurred on the fault.
Fault Plane Solution	Similar in appearance to a focal mechanism, but the data are representative of a population of faults being acted on by one fault system. The nodal planes are therefore best-fit nodal planes based on the data from the focal mechanisms of multiple related events.
Stress ratio	Calculated based on the relative values of principal stresses. It is solved for with the following equation: $$\phi = \frac{\sigma_2 - \sigma_3}{\sigma_1 - \sigma_3} \qquad \text{(eq. 1)}$$ Where $0 > \phi > 1$. A value of 0 is indicative of uniaxial compression (where $\sigma_2 = \sigma_3$) and a value of 1 is indicative of uniaxial tension (where $\sigma_1 = \sigma_2$).
Strain	Changes in the shape and volume of a rock due to tectonic stresses.
Seismic Strain Axes	The strain ellipsoid (an imaginary, deformed sphere) is defined by the orientation and magnitude of the seismic strain axes (which are closely related to the kinematic axes). For the purpose of this study, the largest seismic strain axis is referred to as the X-seismic strain axis, the smallest is referred to as the Z-seismic strain axis, and the intermediate is referred to as the Y-seismic strain axis.

Various earthquake magnitude scales can be used to quantify the intensity of a seismic event – four of which are applicable to this study (Table 3.2). The magnitudes of the majority of seismic data used in this study were recorded as body-wave magnitudes (m_b). However, some of the seismic events from other sources had magnitudes recorded in different scales, such as the surface-wave magnitude scale (M_s). These various forms of earthquake magnitudes were converted into seismic moments (M_o) described in section 5.0.

Table 3.2: Definitions of three earthquake magnitude scales that are referred to in this study. (U.S. Geological Survey, 2012).

Body-wave magnitude (m_b)	Calculated from the amplitude and period of waves traveling through the ground, the distance between the epicenter and station where it was recorded, as well as the depth of the hypocenter of the earthquake.
Surface-wave magnitude (M_s)	Measured from the waves that travel from the hypocenter along layers close to the surface of the earth. It is measured from the Rayleigh waves.
Seismic moment (M_o)	A measurement of energy that occurs from a specific seismic event. It is based on the area of the rupture plane (A), the amount of slip along the fault plane (D), and the amount of force required to cause the slip (μ) in the form of the following equation: $$M_o = \mu AD \qquad (eq.\ 2)$$
Moment magnitude (M_w)	Based on the concept of the seismic moment (M_o). It is the most commonly used scale for earthquake measurement as it is applicable to all magnitudes.

3.3 Fault Slip Inversion and Kinematic Analysis

Fault slip inversion was implemented for each geographical area (Fig. 1.2) to analyse if and how the state of stress varies along the Orogen. Fault slip inversion determines the orientations and relative magnitudes of the principal stresses from seismic data. The relative magnitudes of the principal stresses are used to reconstruct the stress ellipsoid which provides information on the seismic strain of a particular region (Fossen, 2010). The objective of fault slip inversion is to determine a best-fit stress tensor for a population of faults that have random orientations (Zaholar & Vabrec, 2007).

Kinematic analysis involves calculating the orientations of the P- and T-axes based on the orientations of the nodal planes for each seismic event. On a stereographic

projection the P- and T-axes are symmetry axes, located in the center of the P- and T-sectors (Fossen, 2010). This approach was applied to all seismic data from each region based on the focal mechanism solutions for each seismic event. A fault plane solution was then created by calculating the best-fit nodal planes for the entire population of fault data.

Both fault slip inversion and kinematic analysis require that the data satisfy the following assumptions:

1) The direction of movement and the shear stress along the fault are parallel.

2) The lithologies in the region are homogeneous so that the stress field is not affected by rock type.

3) The stress field for each region must be uniform, and faults do not interact or affect each other.

4) No significant rotation of the fault block has occurred since the deformation event.

(Fossen, 2010).

The five regions that were studied are extensive, and it is evident that the stress fields are not consistent throughout. It is therefore necessary to interpret the diagrams obtained from this study in light of the assumptions listed above. However, because the fault data are heterogeneous, two methods were used to separate the heterogeneous fault data into homogeneous subgroups. The first method involved manual separation of the data in each region based on the orientations of the nodal planes, corresponding slip directions, and general sense of movement (normal, thrust, strike slip). The second involved the use of the Gauss method (described in Zalohar and Vabrec (2007)). The Gauss method involves finding the optimal stress tensor for each homogeneous subgroup of faults within the population. The best-fit stress tensor is based on the amount of angular misfit

between the direction of movement on the fault plane and the actual, resolved direction of movement, and the normal stress to shear stress ratio acting on the fault plane. These factors contribute to the object function, which is maximized to find the best-fit stress tensor for each homogeneous subgroup of faults (Zalohar & Vabrec, 2007).

3.3.1 Slip Direction and Overall Sense of Movement

The dominant types of movement (normal, reverse, strike-slip, etc.) occurring on the subgroups of faults in each area were determined by analysing three types of stereographic projections. The first diagram plotted the nodal planes and slip directions, the second plotted the P- and T-axes, and the third was a depiction of the fault plane solutions.

For each region, the nodal planes were plotted on a stereographic projection. Clusters of nodal planes showed the dominant trends in the strikes of the fault planes for each region. This projection also showed the degree that the fault planes were dipping. An arrow representing the slip direction of the hanging wall relative to the footwall was plotted next to the corresponding fault planes to illustrate the direction of movement (Fig. 3.1).

The orientation (trend and plunge) of the compressive (P-) and the tensile (T-)
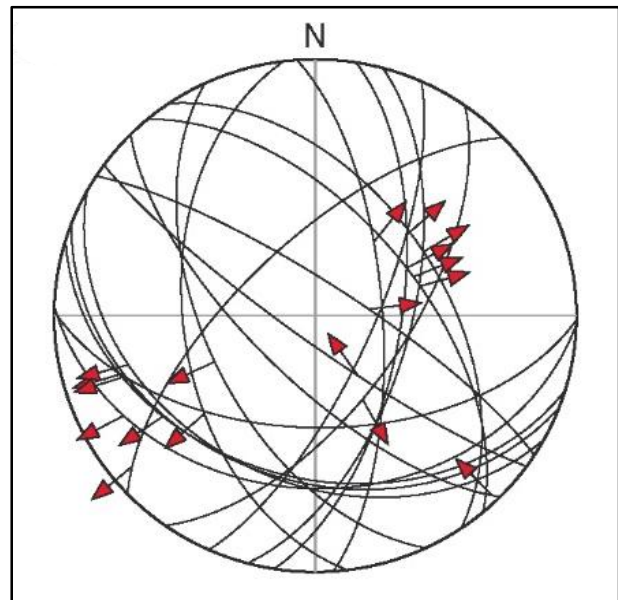
Figure 3.1: Example of fault planes plotted on a stereographic projection as great circles. This example shows a random orientation of moderately dipping normal faults. The slip-direction arrows attached to each fault plane show that the majority of the planes display hanging wall movement downwards towards the NE and SW. (From Fossen, 2010).

axes were plotted as symmetry axes in the centre of the P- and T-sectors, respectively, which are in turn defined by the orientations of the nodal planes. The cluster of P-axes shows the general orientation of the majority of compressive stress, and the cluster of T-axes shows the general orientation of the majority of tensile stress (Fossen, 2010). This information helps to define the sense of movement that occurred on the fault planes because it can be used to create the fault plane solutions.

This orientations of the P- and T-axes were used to define the best-fit nodal planes which are represented in the fault plane solutions for each area. In these diagrams the tensile (T-) sector is shaded and the compressive (P-) sector is white. Fault plane solutions give insight into the general type of movement that occurred along a population of faults
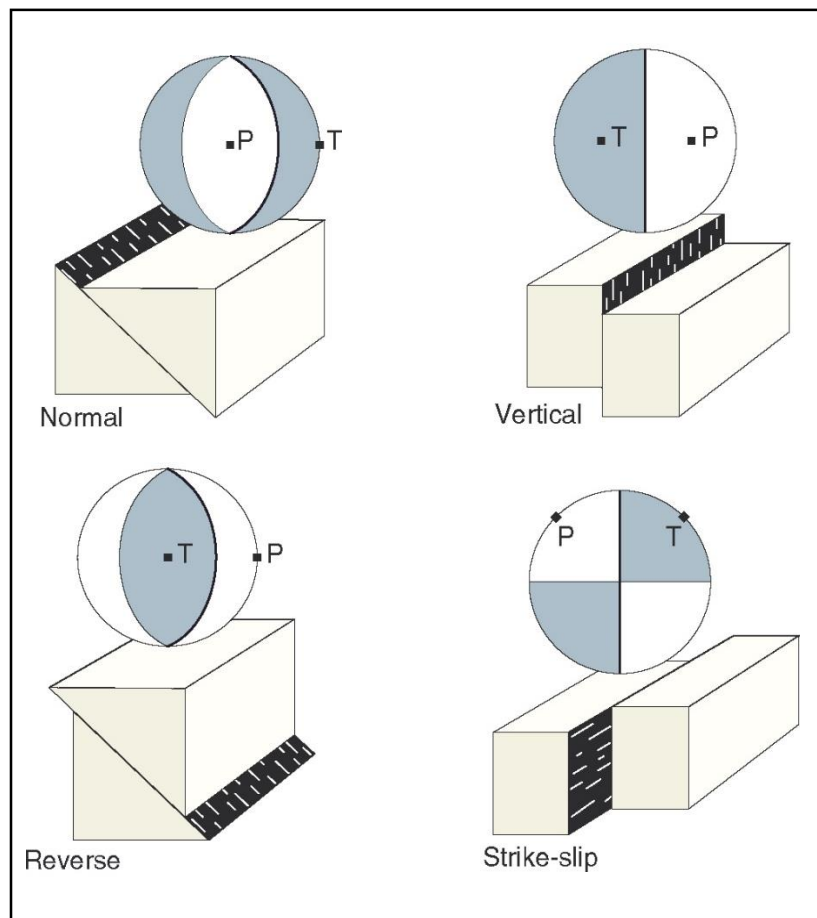
Figure 3.2: Four standard types of fault movement and their corresponding fault plane solutions. Shaded areas represent the tensile (T-) sectors, and white areas represent the compressive (P-) sectors. Bolded lines denote the fault plane, and non-bolded lines denote the orthogonal plane. (From Fossen, 2010).

under a particular stress regime; however, they do not indicate along which of the two nodal planes the fault slip has occurred. Normal, thrust, and strike-slip faults have characteristic fault plane solutions (Fig. 3.2) (Fossen, 2010).

3.3.2 Principal Stresses and the Stress Ellipsoid

Tangent lineation is a representation of the movement of the footwall relative to the hanging wall. It is calculated by plotting the fault plane and its lineation on a stereoplot, and then by creating the M-plane (which passes through the lineation and the pole to the fault plane) (Fig. 3.3). The tangent lineation is an arrow on the plot that is tangent to the M-plane and located at the pole to the fault plane. Patterns of tangent lineations for a population of fault data can provide information on the relative sizes of the principal stresses that form the stress ellipsoid for the area. From this information, the stress regime can be interpreted as uniaxial tension ($\phi = 1$), uniaxial compression ($\phi = 0$), or something in between ($0 < \phi < 1$) (Fig. 3.4) (Fossen, 2010).
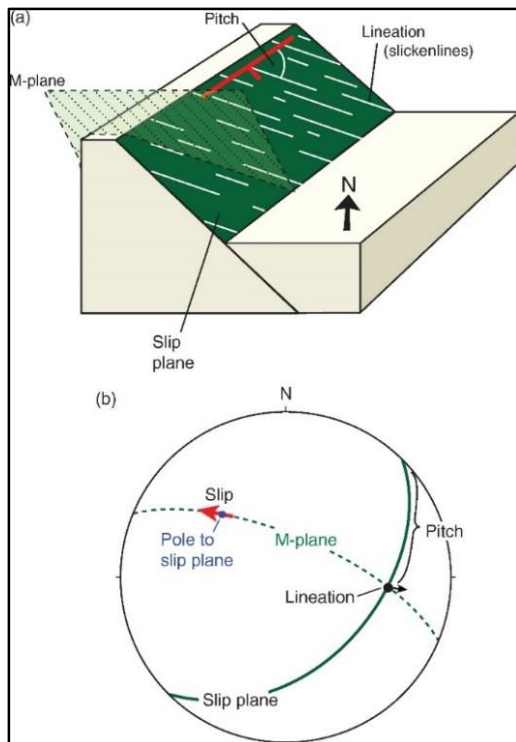
Figure 3.3: A schematic (a) and stereographic (b) representation of the orientation of lineation/pitch on a fault plane. The schematic diagram (a) shows an oblique (sinistral) normal fault. The stereographic projection (b) shows that the tangent lineation is plotted at the pole of the fault plane, tangent to the M-plane. It shows that the footwall is moving up towards the west, relative to the hanging wall (From Fossen, 2010).
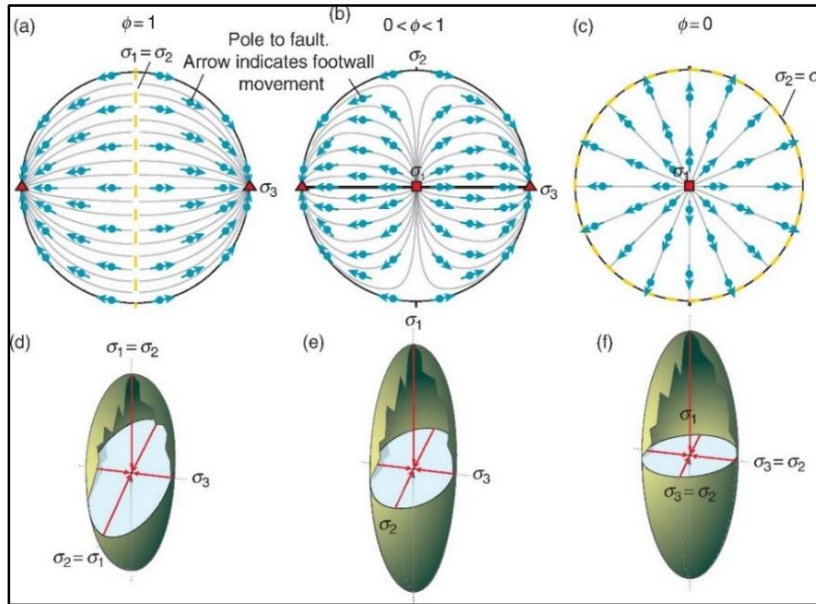
Figure 3.4: (a), (b), and (c) show idealized stereographic projections of tangent lineation diagrams with various stress ratios (φ), and the corresponding shape of the stress ellipsoid ((d), (e), and (f) respectively). Complete uniaxial tension is illustrated by (a) and (d), and complete uniaxial compression is represented by (c) and (f) (From Fossen, 2010).

Mohr diagrams plot the average principal stresses (σ_1, σ_2, and σ_3) for a fault population on a horizontal axis that measures the normal stress (σ_n), while the vertical axis represents the shear stress (σ_s) (Fig. 3.5). For this study, the Mohr diagrams are dimensionless and illustrate the relative values of the principal stresses because absolute values were not obtained. From the relative values of the principal stresses the value of the stress ratio (φ) can be calculated. T-Tecto (Version 3.0) was used to create the Mohr diagrams based on the orientations of the nodal planes and the lineations. The largest principal stress (σ_1) from each seismic event is plotted as a point on the diagram for a fault population. On these diagrams, the distance between σ_1 and σ_3 gives the differential stress of the system, and also defines the diameter of the Mohr circle. Defining the Mohr circle provides a method of illustrating how normal and shear stresses from the fault populations affect the body of rock at a specific point (Fossen, 2010).
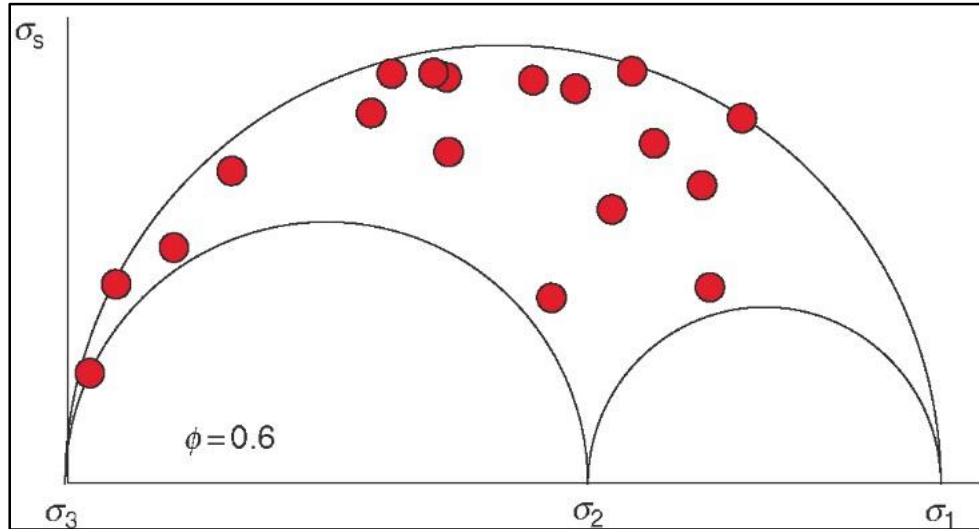
Figure 3.5: Example of a Mohr diagram for a fault population. The relative values of principal stresses (σ_1, σ_2, and σ_3) are plotted along the x-axis which represents the normal stress (σ_n). The y-axis represents the shear stress (σ_s). The stress ratio (ϕ) is calculated by eq. 1. The points on the diagram (red circles) represent the largest principal stress (σ_1) for each seismic event. (From Fossen, 2010).

3.3.3 Seismic Strain Axes and the Strain Ellipsoid

The orientation (trend and plunge) of the kinematic axes for each area were calculated. The kinematic axes are directly related to the seismic strain axes that define the strain ellipsoid. The seismic strain axes are represented as X, Y, and Z, from largest to smallest seismic strain respectively. The intermediate strain axis (Y) therefore plots at the intersection of the nodal planes, while the X and Z strain axes plot in the center of the P- and T-sectors respectively on a fault plane solution (Fossen, 2010). Although the magnitudes of the strain axes were not obtained, the seismic strain axes were plotted on a stereoplot to provide a depiction of the orientation of the strain ellipsoid for each area.

4.0 Results

The data from each area were grouped into subpopulations based on fault regimes (normal, thrust, and strike-slip faults) both manually, and by use of the Gauss method. In some areas, the subpopulations were composed of a limited amount of data due to a lack of seismic events with complete focal mechanisms presently available from the catalogues; however, the fault regimes were different enough to justify separating the data into these subgroups. This chapter describes the results of the crustal stress and seismic strain analyses performed on each of the five geographical areas (Fig. 1.2).

4.1 Normal Fault Regime

Seismic events from normal faulting are present across the entire Himalayan Orogen (from areas 1-4), but not in the Shillong Plateau region (area 5). Normal faulting events are increasingly prevalent towards the eastern regions (particularly areas 3 and 4). The orientations of the nodal planes are better constrained in areas 1 through 3 than they are in area 4. In areas 1-3 the nodal planes trend N-S and have moderate dip angles. This same trend is visible in area 4, although the strikes and dips of the nodal planes are slightly more varied (Fig. 4.1). The fault plane solutions for each region show best-fit nodal planes striking consistently N-S with moderate dip angles (Fig. 4.2). For all four areas, the P-axes trend vertically, while the T-axes are close to horizontal in the E-W direction (Fig. 4.3). This is indicative of horizontal E-W extension that is well-supported by the tangent lineation diagrams which show the footwalls moving east and west relative to the hanging walls (Fig. 4.4). The seismic strain axes reinforce the results from the normal faulting regime, showing that in all four areas the largest strain axis (the X-axis) is sub-horizontal, trending in the E-

W direction, the intermediate strain axis (the Y-axis) is also sub-horizontal, trending in the

N-S direction, and the smallest strain axis (the Z-axis) is sub-vertical. The orientations of

these axes does not vary significantly along strike of the Orogen (Fig. 4.5). The Mohr

diagrams illustrate the stress ratio values (ϕ) for the normal faulting events in each area

(Fig. 4.6). In the region furthest west, the stress ratio value was calculated to be $\phi = 0.5$,

indicating that the stress ellipsoid is defined by unequal principal stresses (Fig. 3.4 (b) and

(c)). Areas 2, 3, and 4 all have stress ratio values of $\phi = 0.3$, which also indicates that the

principal stresses are unequal; however, it is closer to the conditions of uniaxial

compression (Fig. 3.4 (c) and (f)).

Overall, the stresses and resultant strain acting on the faults in the normal fault

regime were consistent in orientation from areas 1-4, as illustrated by the stereoplots and

Mohr diagrams constructed from fault slip inversion (Table 4.1).
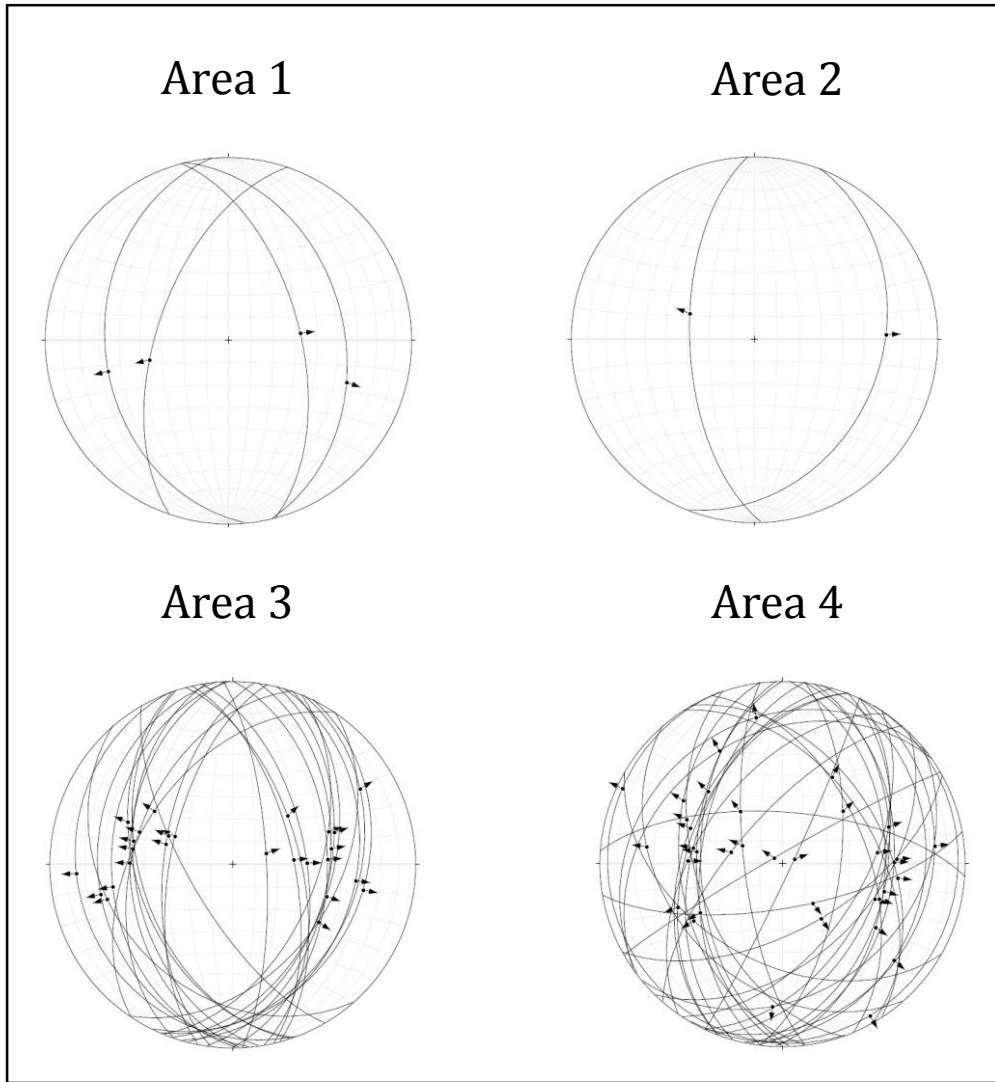
Figure 4.1: Nodal planes and the direction of slip for all seismic events of the normal fault regime from areas 1-4. (There were no seismic events belonging to the normal fault regime in area 5). Nodal planes are represented as great circles and the corresponding direction of slip of the hanging wall relative to the footwall is represented as the arrow attached to the great circle. The nodal planes of the normal faults show a consistent N-S strike and moderate dip in areas 1-3. Area 4 contains nodal planes with more varied orientations, but shows that the movement of the hanging wall relative to the footwall is still dominantly in the E-W orientation.

Figure 4.2: Fault plane solutions for all seismic events of the normal fault regime in areas 1-4. (There were no seismic events belonging to the normal fault regime in area 5). Best-fit nodal planes are represented by great circles, shaded areas represent the tensile (T-) fields, and white areas represent the compressive (P-) fields. For the normal fault regime, all areas along the Orogen (1-4) exhibit best-fit nodal planes that trend N-S with moderate dip angles.

Figure 4.3: Compressive (P-) and tensile (T-) axes of all seismic events of the normal fault regime in areas 1-4. (There were no seismic events belonging to the normal fault regime in area 5). T-axes are represented by red dots and P-axes are represented by blue dots. In all areas with normal faulting (1-4) the P-axes trend vertically, while the T-axes trend sub-horizontally in the E-W orientation.

Figure 4.4: Tangent lineations for all seismic events of the normal fault regime in areas 1-4. (There were no seismic events belonging to the normal fault regime in area 5). The lineations show that the movement of the footwall relative to the hanging is predominantly in the E-W orientation for the four areas.

Figure 4.5: Seismic strain axes depicting the orientations of the axes of the strain ellipsoid for all seismic events of the normal fault regime in areas 1-4. (There were no seismic events belonging to the normal fault regime in area 5). The largest strain axis (the X-axis) is represented by the red circle, the smallest strain axis (the Z-axis) is represented by the blue circle, and the intermediate strain axis (the Y-axis) is represented by the green circle. Areas 1-4 have similar kinematic axes in that the Z-strain axis is vertical, the X-strain axis is horizontal and trending roughly E-W, and the Z-strain axis is also horizontal but trending roughly N-S.

Figure 4.6: The stress ratio values (Φ) and corresponding dimensionless Mohr diagrams for the normal fault regime in areas 1-4. (There were no seismic events belonging to the normal fault regime in area 5). Area 1 has a stress ratio value of Φ = 0.5 which corresponds to unequal principal stresses, also illustrated in Figure 3.4 (b) and (e). Areas 2, 3, and 4 have stress ratio values of Φ = 0.3 which corresponds to unequal principal stresses as well, but closer to uniaxial compression conditions such as those shown in Figure 3.4 (c) and (f).

Table 4.1: A summary of the key stress and strain characteristics of the normal faulting events for areas 1-4 (there were no normal faulting events in area 5). The orientations of both the best-fit nodal planes and the horizontal strain axes do not vary significantly from west to east (areas 1-4) along the Orogen. The stress ratio value is relatively consistent from west to east as well, corresponding to a stress ellipsoid defined by unequal principal stresses to uniaxial compression.

		Area 1	Area 2	Area 3	Area 4	Area 5
Normal Fault Regime	Best-Fit Nodal Plane Orientations	N-S	NNE-SSW	N-S	NNE-SSW	No events
	Stress Ratio Value	φ = 0.5	φ = 0.3	φ = 0.3	φ = 0.3	
	Horizontal Strain Axis Orientations	← →	← →	← →	← →	

4.2 Thrust Fault Regime

Seismic events of the thrust fault regime were present across the entire Himalayan Orogen (from areas 1-4), but not in the Shillong Plateau region (area 5). Thrust fault events were much more prevalent in area 4, and least prevalent in area 3. Furthermore, the orientations of the nodal planes were better unwavering in areas 1 through 3 compared to area 4. In areas 1 and 2, the nodal planes are mainly striking NW-SE, with one set of nodal planes dipping steeply to the south and the other set dipping shallowly to the north. In areas 3 and 4 the strike of the nodal planes is roughly E-W, but the dip angles remain the same with one set dipping steeply to the south and the other dipping shallowly to the north (Fig. 4.7). Similarly, the best fit nodal planes of the fault plane solutions progressively

rotate from striking NW-SE to striking E-W when moving from areas 1-4 respectively (Fig. 4.8). In all four areas, the T-axes trend vertically, while the P-axes are sub-horizontal. In areas 1 and 2 the P-axes trend NE-SW, and in areas 3 and 4 the P-axes are varied (Fig. 4.9). These trends are reinforced by the horizontal NE-SW to N-S compression apparent in the tangent lineation diagrams (Fig. 4.10). The seismic strain axes further support this analysis by illustrating that the largest strain axis (the X-axis) is sub-vertical in all four areas, while the smallest strain axis (the Z-axis) is sub-horizontal but changes in orientation from NW-SE to E-W from west to east along the Orogen (Fig. 4.11). The stress ratio values vary from ϕ = 0.2 in the west (area 1) to ϕ = 0.8 in the east (area 4) and these varying values are illustrated in the corresponding dimensionless Mohr diagrams (Fig. 4.12). The stress ratio values for the thrust fault regime therefore correspond to stress ellipsoids defined by conditions that range between uniaxial tension and uniaxial compression (Fig. 3.4 (b) and (e)).

In general, when moving from west to east along the Orogen, the trends of the principal stress and strain axes change slightly between areas 2 and 3 (Table 4.2). In areas 1 and 2, the dominant trend of compression (represented by horizontal strain axes) is in the NE-SW direction, while in areas 3 and 4 the dominant trend of compression is in the N-S direction.
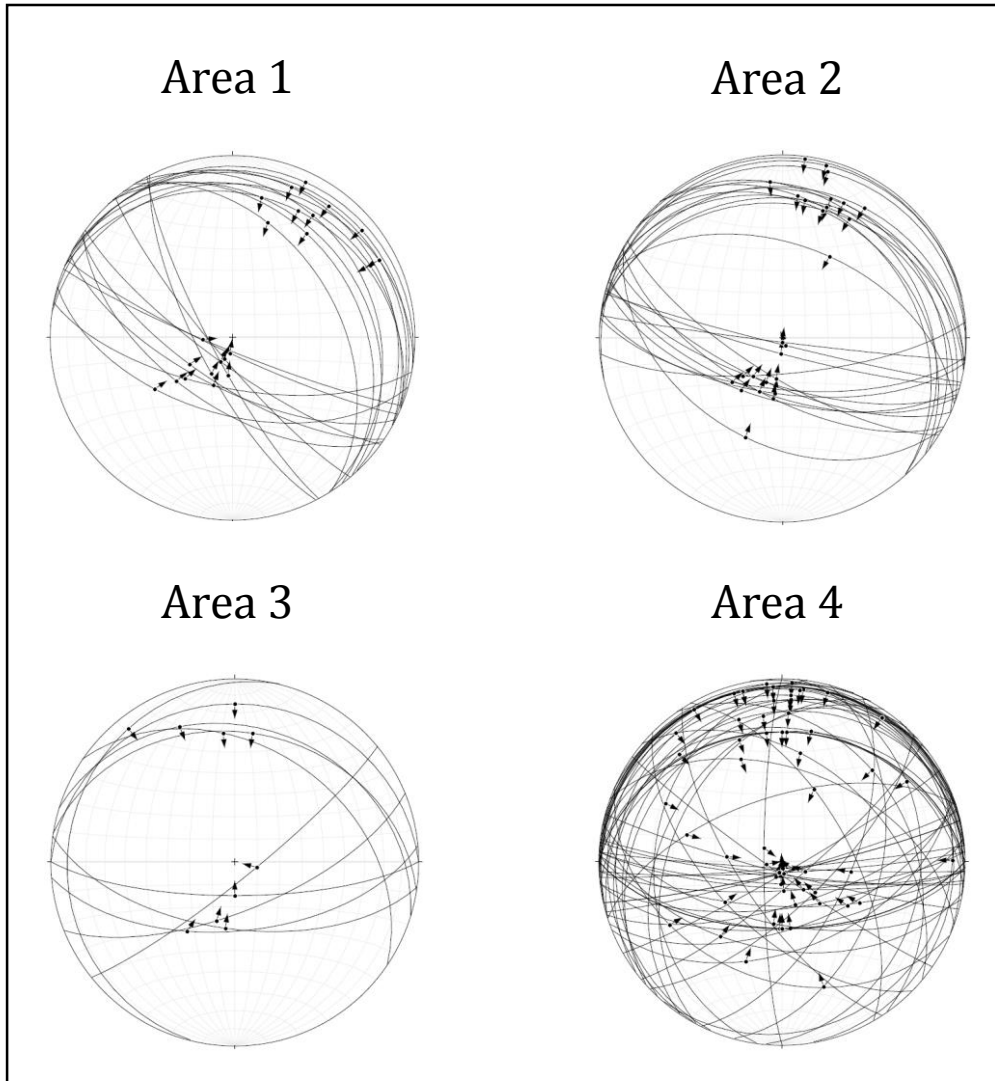
Figure 4.7: Nodal planes and the direction of slip of the hanging wall relative to the footwall for all seismic events of the thrust fault regime from areas 1-4 (there were no seismic belonging to the thrust fault regime in area 5). Nodal planes are represented as great circles and the corresponding direction of slip is represented as the arrow attached to the great circle. Areas 1 and 2 have well-constrained orientations of nodal planes in the NW-SE direction. The nodal planes in area 3 are also well-constrained but oriented roughly E-W. Area 4 has nodal planes with varied orientations, but a general trend in the E-W direction as well. In all four areas there is consistently a cluster of nodal planes dipping steeply to the south, and another cluster of nodal planes dipping shallowly to the north.
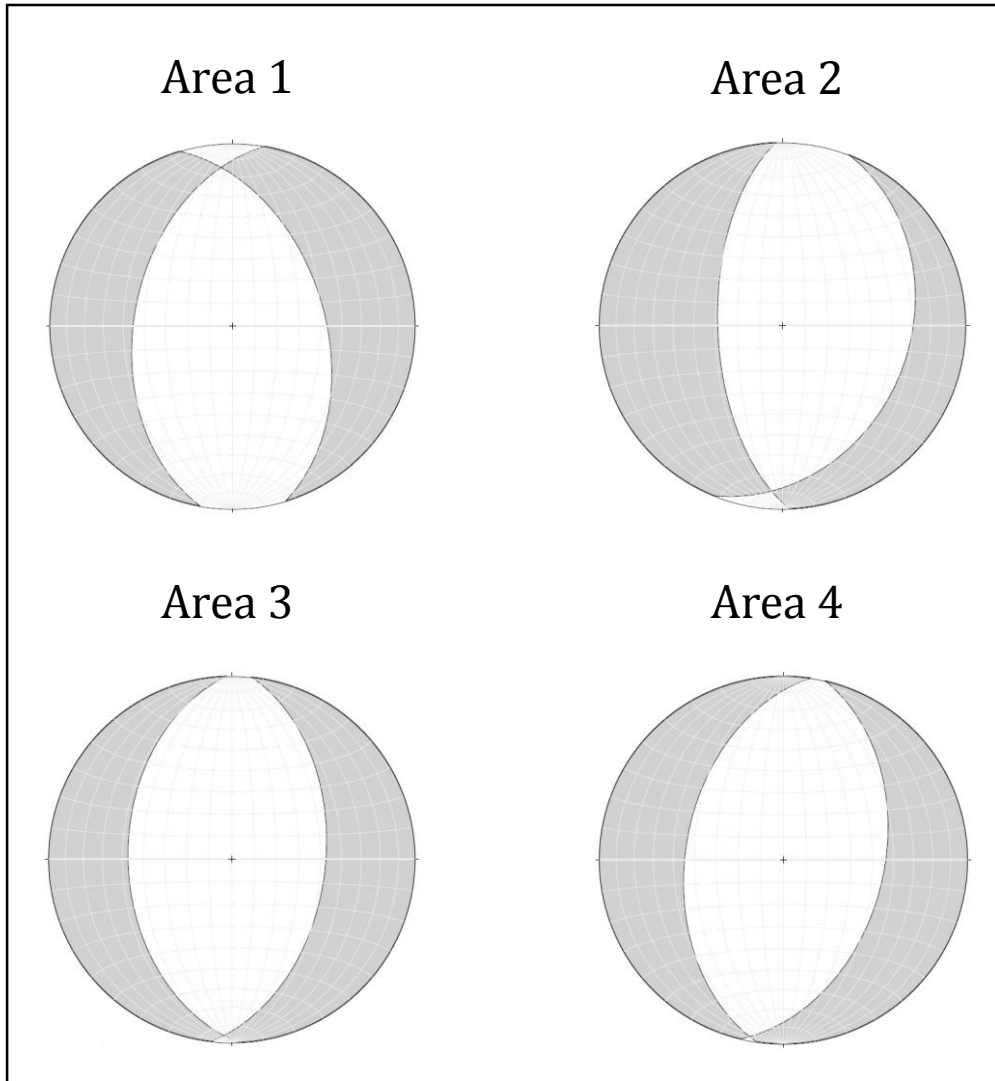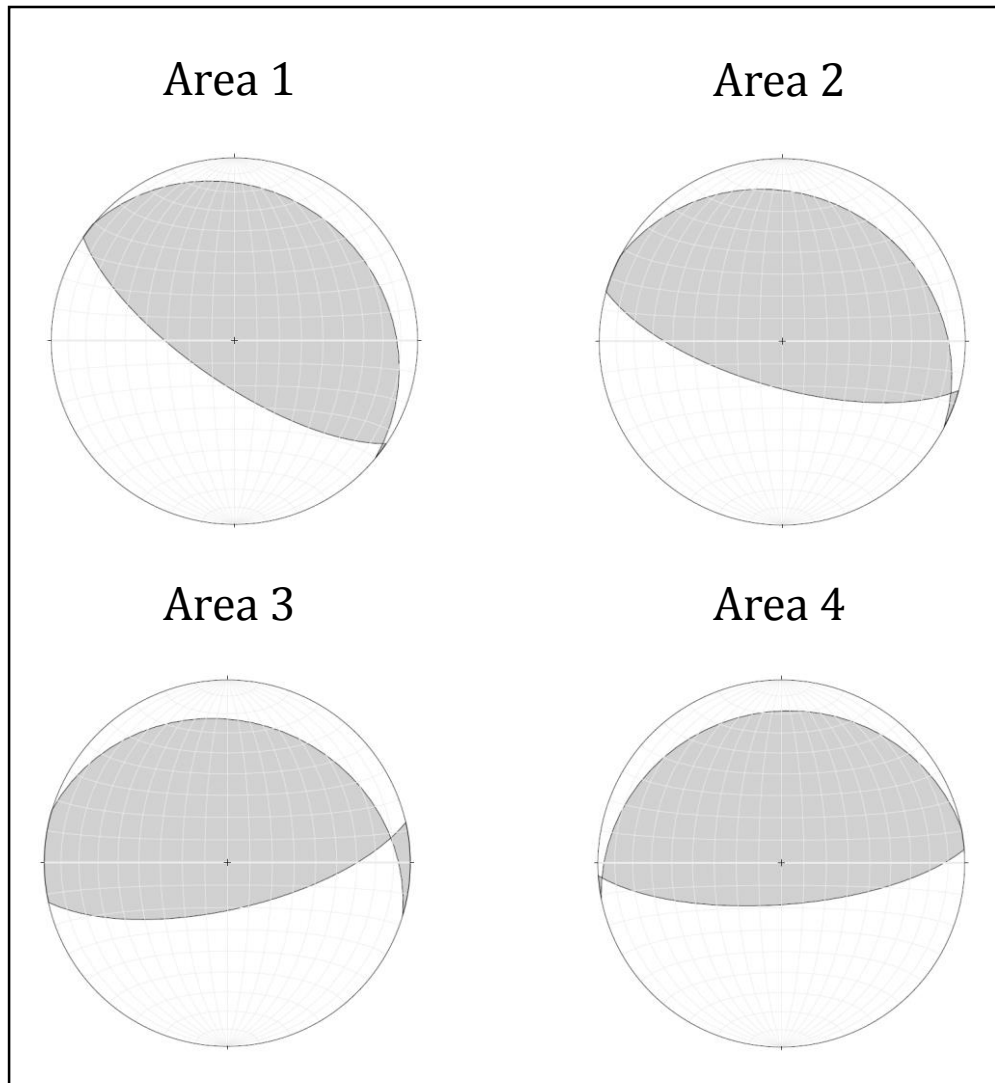
Figure 4.8: Fault plane solutions for all seismic events of the thrust fault regime in areas 1-4. (There were no seismic events belonging to the thrust fault regime in area 5). Best-fit nodal planes are represented by great circles, shaded areas represent the tensile (T-) fields, and non-shaded areas represent the compressive (P-) fields. The orientations of the best-fit nodal planes changes from areas 1 and 2 in the NW-SE direction, to areas 3 and 4 in the E-W direction. All four areas have one best-fit nodal plane dipping steeply towards the south and another best-fit nodal plane dipping shallowly to the north.
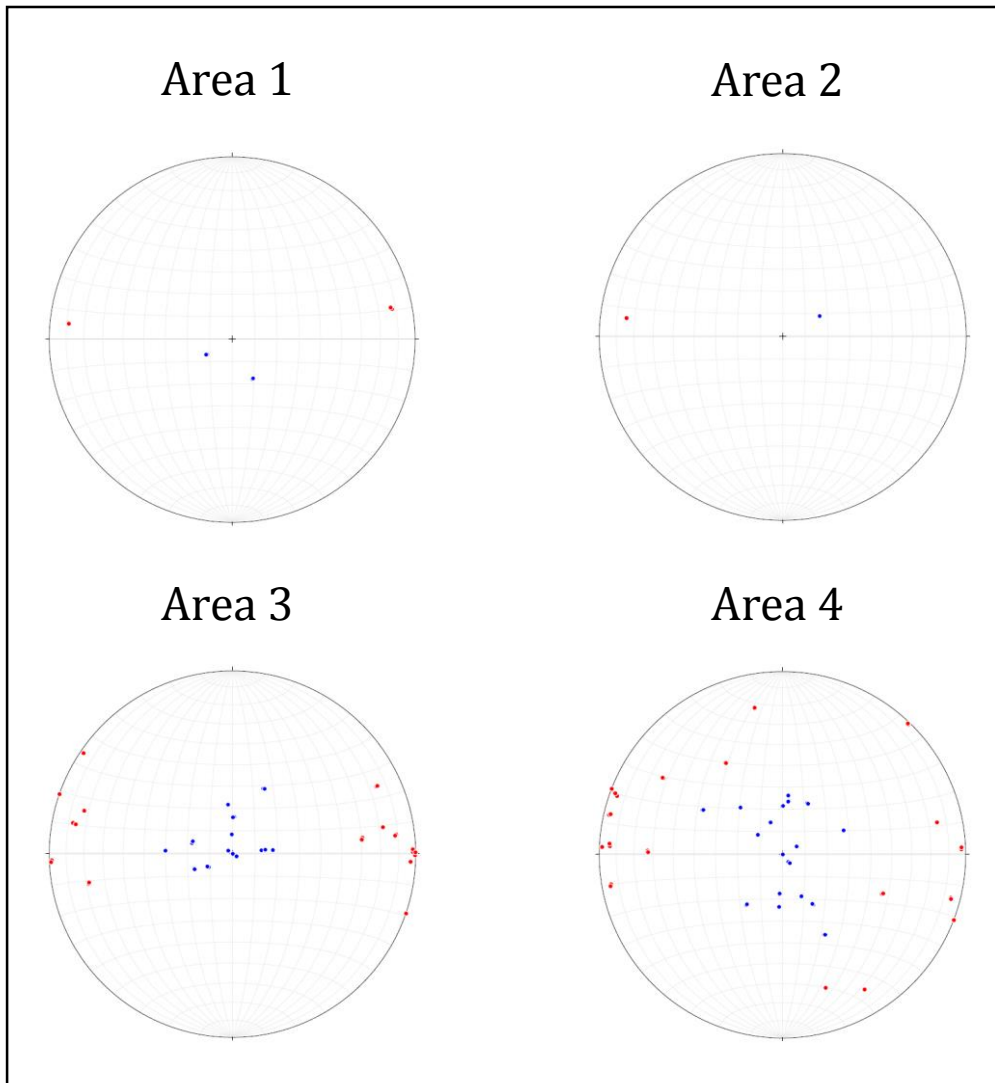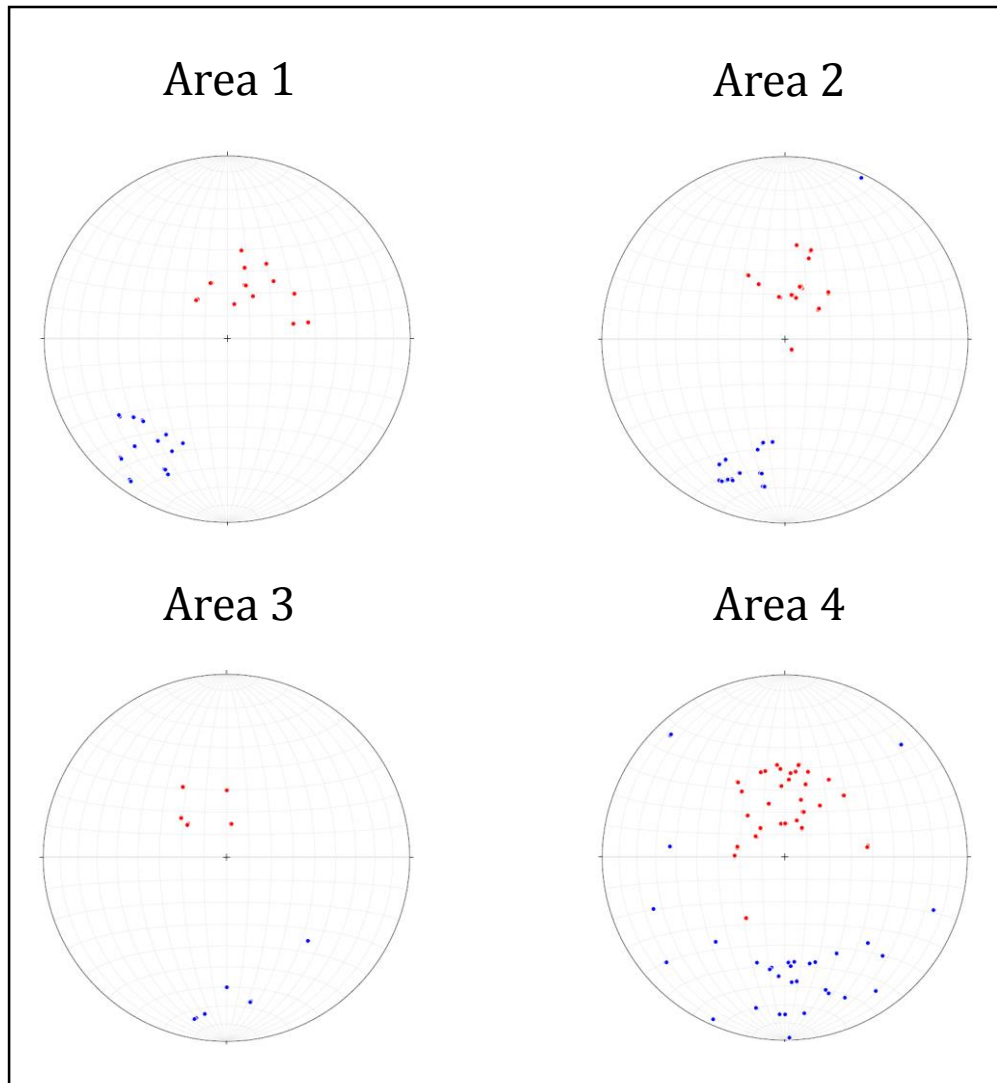
Figure 4.9: Compressive (P-) and tensile (T-) axes of all seismic events of the thrust fault regime in areas 1-4. (There were no seismic events belonging to the thrust fault regime in area 5). T-axes are represented by red dots and P-axes are represented by blue dots. In areas 1-4 the T-axes trend sub-vertically. In areas 1 and 2 the P-axes trend sub-horizontally in the SW-NE direction. In areas 3 and 4 the P-axes also trend sub-horizontally but in a less-defined orientations.
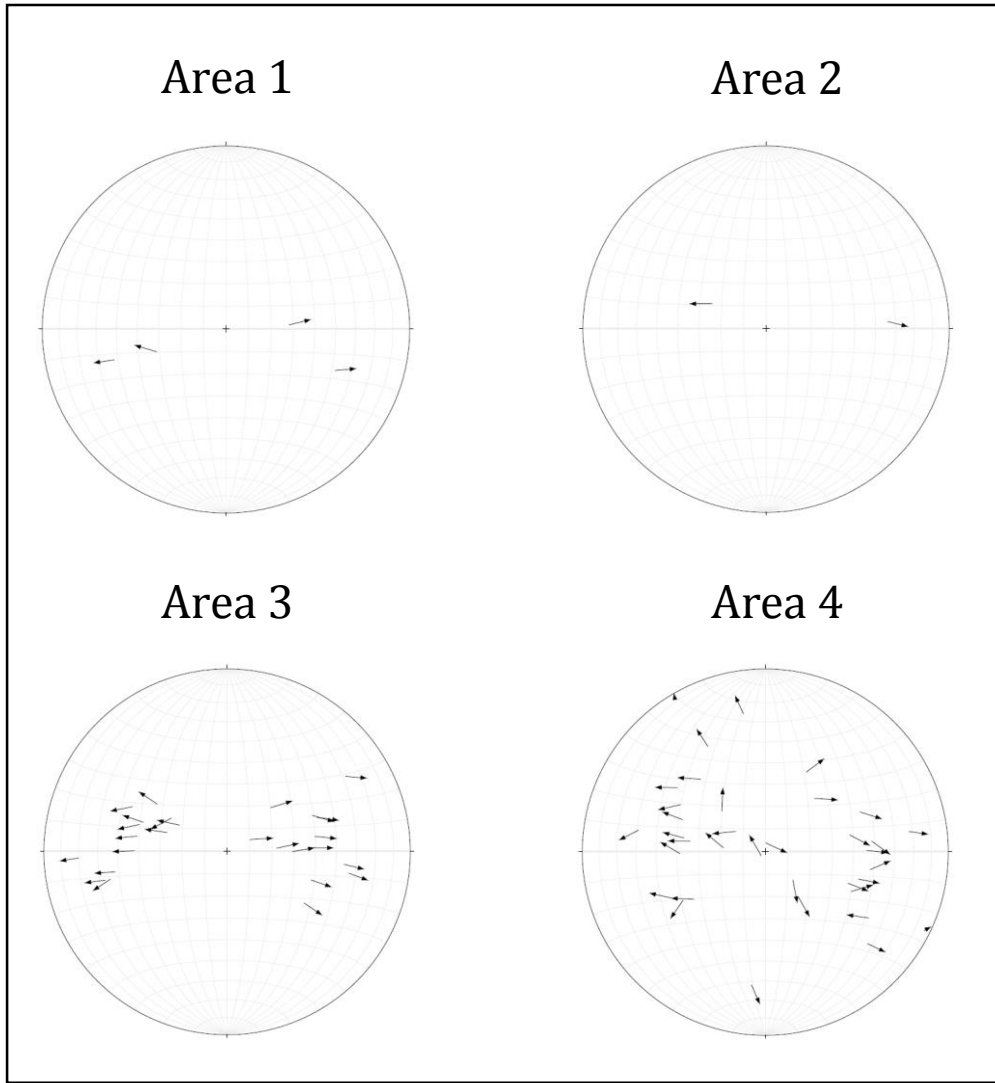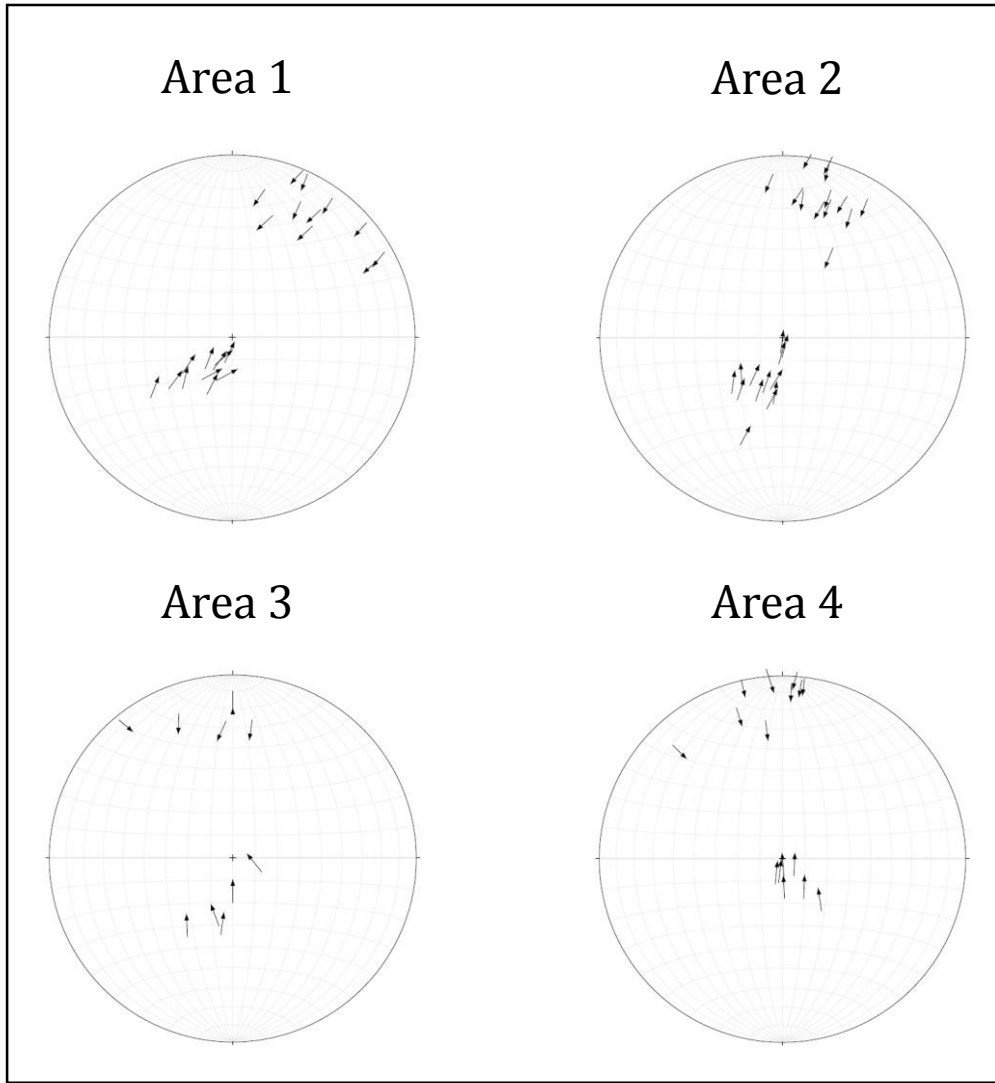
Figure 4.10: Tangent lineations for all seismic events of the thrust fault regime in areas 1-4. (There were no seismic events belonging to the thrust fault regime in area 5). The directions of the arrows correspond to the movement of the footwall relative to the hanging wall. The diagrams above represent compressive movement in the NE-SW direction (areas 1 and 2) to the N-S direction (areas 3 and 4).
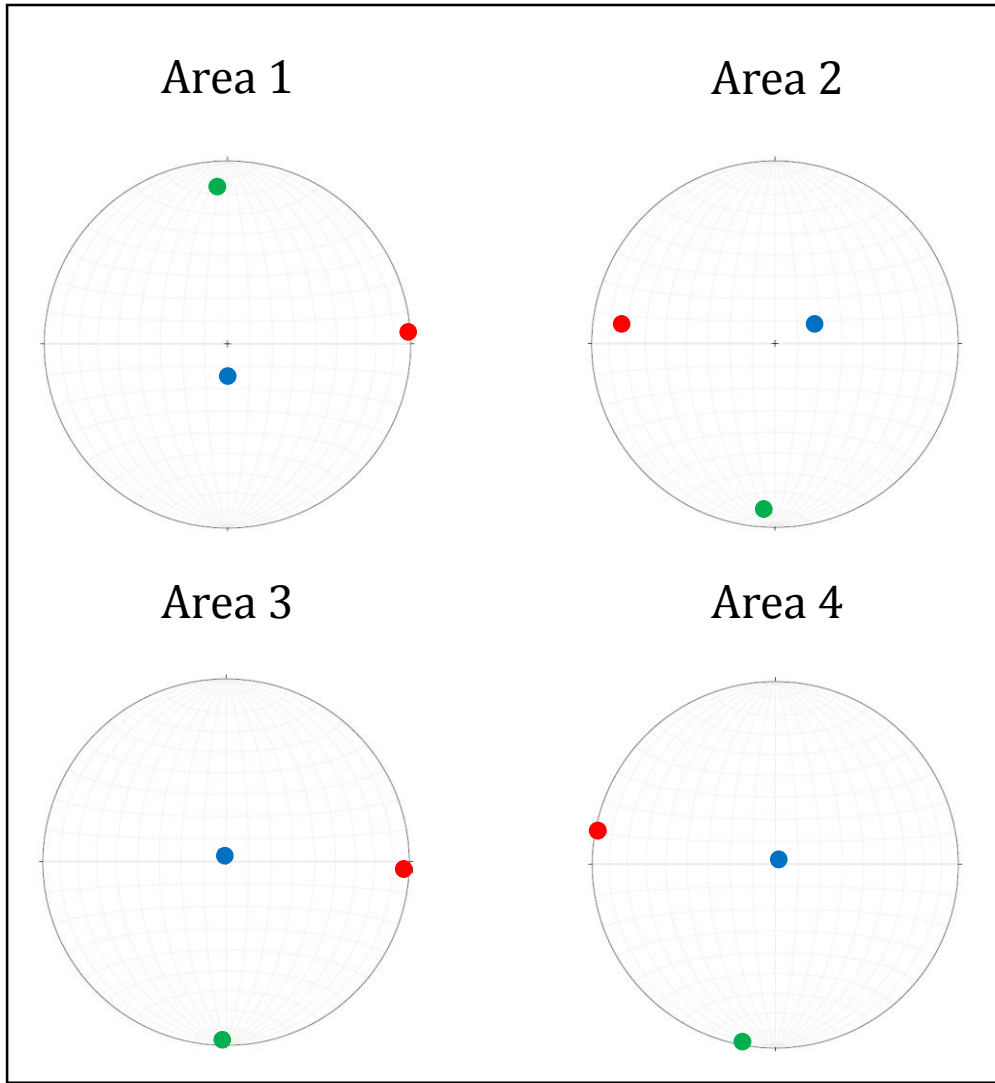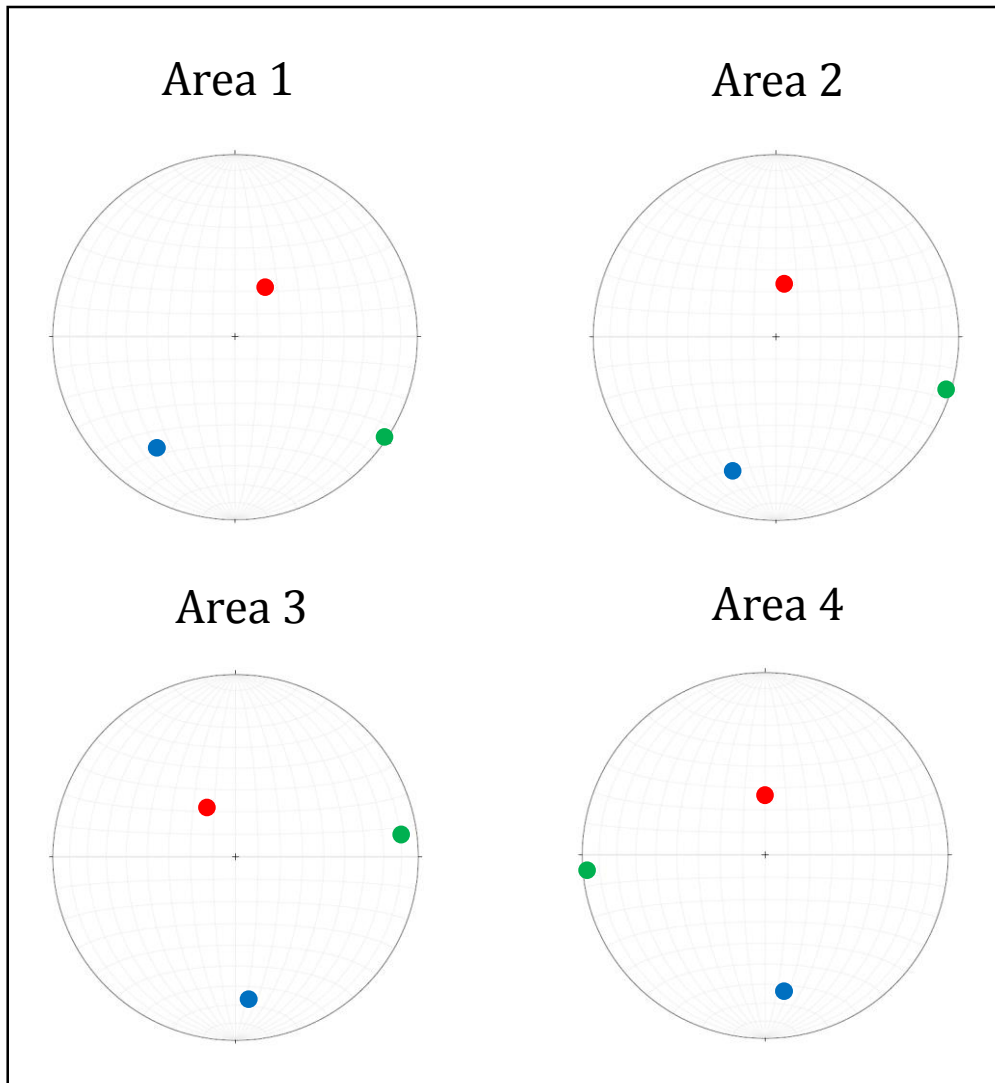
Figure 4.11: Seismic strain axes depicting the orientations of the axes of the strain ellipsoid for all seismic events of the thrust fault regime in areas 1-4. (There were no seismic events belonging to the thrust fault regime in area 5). The largest strain axis (the X-axis) is represented by the red circle, the smallest strain axis (the Z-axis) is represented by the blue circle, and the intermediate strain axis (the Y-axis) is represented by the green circle. In all four areas, the X-strain axis is sub-vertical, while the Z-strain axis changes in orientation from NE-SW in the western regions to N-S in the eastern regions.
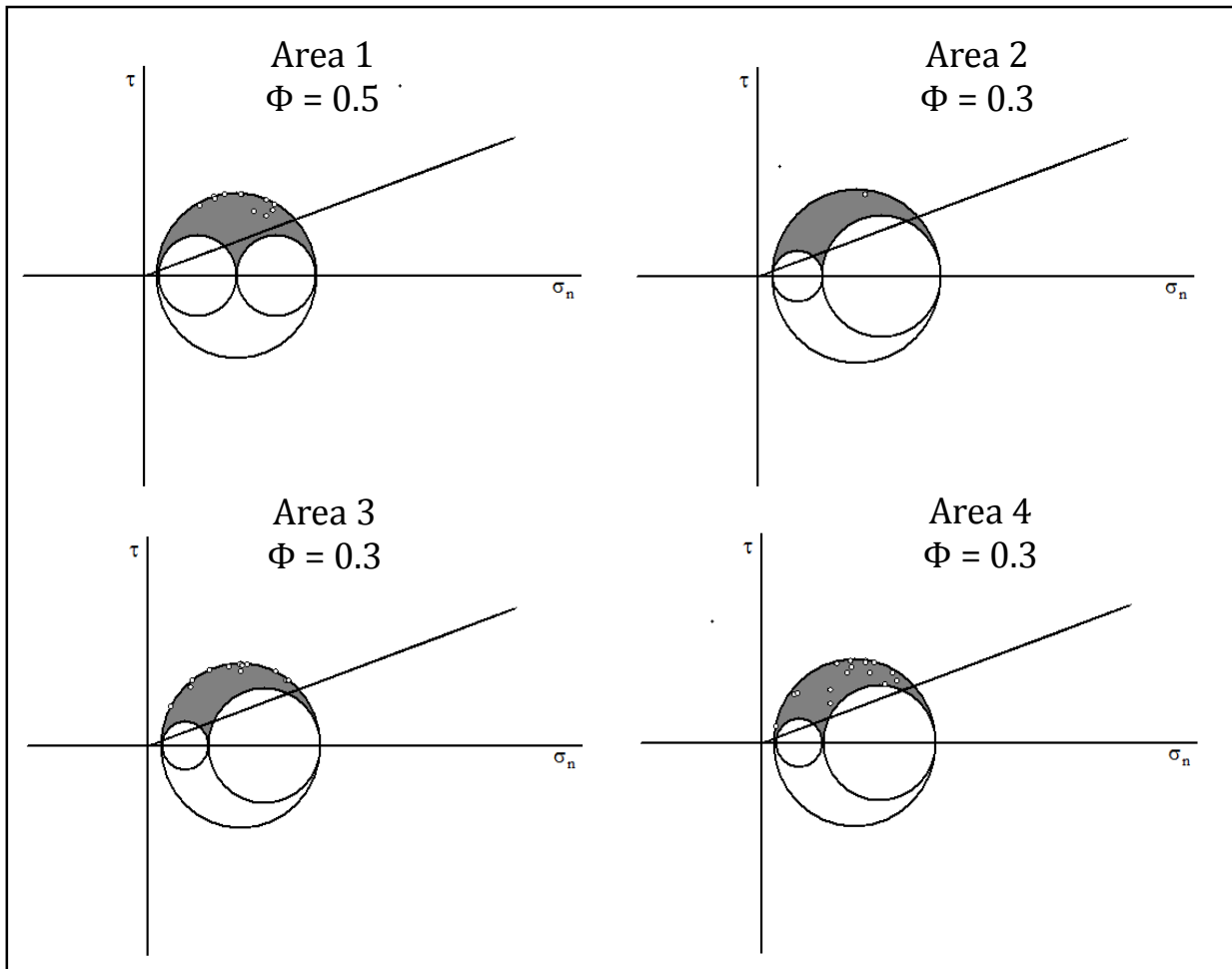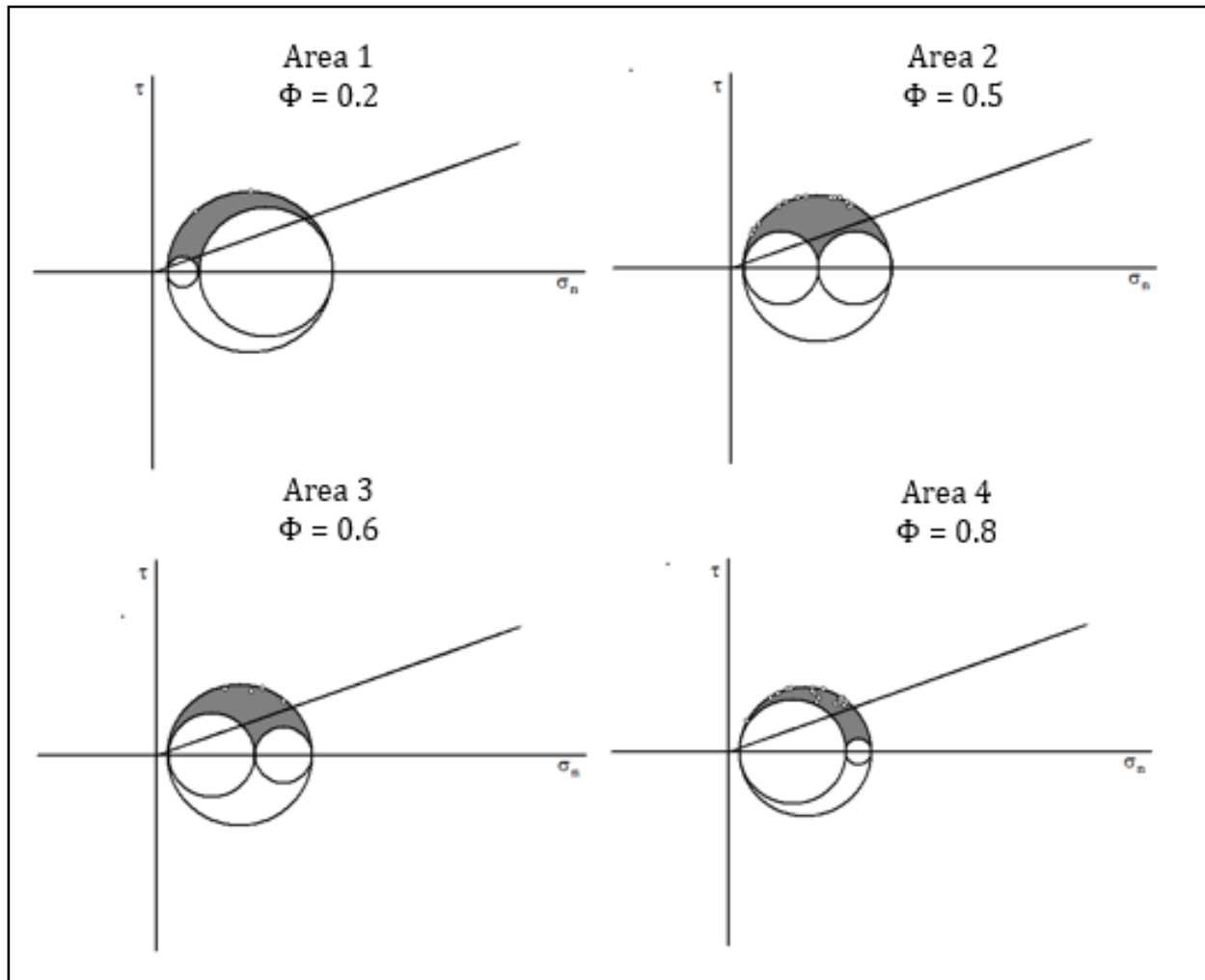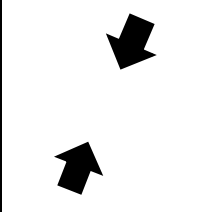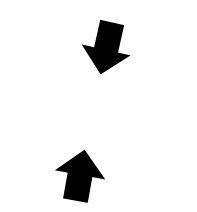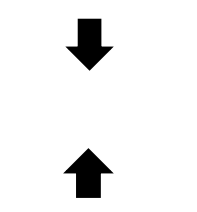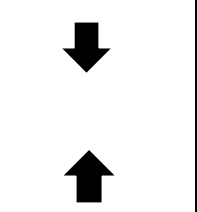
Figure 4.12: The stress ratio values (Φ) and corresponding dimensionless Mohr diagrams for the thrust fault regime in areas 1-4. (There were no seismic events belonging to the thrust fault regime in area 5). Area 1 has a stress ratio value of Φ = 0.2 which corresponds closely to uniaxial compression (Fig. 3.4 (c) and (d)). Areas 2, 3, and 4 have progressively higher stress ratio values up to Φ = 0.8, corresponding to unequal principal stress values that define stress ellipsoids between uniaxial tension and uniaxial compression (Fig. 3.4 (b) and (e)).

Table 4.1: A summary of the key stress and strain characteristics of the thrust faulting events for areas 1-4 (there were no thrust faulting events in area 5). The orientations of both the best-fit nodal planes and the horizontal strain axes vary from a NE-SW orientation in the western regions (areas 1 and 2) to an N-S orientation in the eastern regions (areas 3 and 4). The stress ratio values increase progressively from west to east along the Orogen, defining stress ellipsoids with unequal principal stresses. The stress ratio in area 1 is representative of a stress ellipsoid close to uniaxial compression (Fig. 3.4 (f)), while stress ratio in area 4 is representative of a stress ellipsoid close to uniaxial tension (Fig. 3.4 (d)).

		Area 1	Area 2	Area 3	Area 4	Area 5
Thrust Fault Regime	Best-Fit Nodal Plane Orientations	NW-SE	NW-SE	E-W	E-W	No events
	Stress Ratio Value	$\Phi = 0.2$	$\Phi = 0.5$	$\Phi = 0.6$	$\Phi = 0.8$	
	Horizontal Strain Axis Orientations					

4.3 Strike Slip Fault Regime

Seismic events of the strike slip regime were present across the entire Himalayan Orogen (from areas 1-5), and composed all of the events in the Shillong Plateau region (area 5). Strike slip events were most prevalent in the eastern regions, particularly area 4. Furthermore, the orientations of the fault planes were better constrained in areas 3 and 5, and not very well constrained in area 4. The nodal planes of the strike slip events are steeply dipping and show general NE-SW and NW-SE trends that are most evident in areas 3 and 4 (Fig. 4.13). The best-fit nodal planes of the fault plane solutions also trend in the NE-SW and NW-SE orientations. Areas 1 and 2 have a slightly oblique component, although

this observation must be taken in light of the lack of data in these areas (Fig. 4.14). In most of the areas the P- and T- axes are separated into four clusters that correspond to the quadrants defined by the nodal planes in the fault plane solutions; however, the orientations of the P- and T-axes in area 4 are highly variable (Fig. 4.15). The tangent lineation diagrams for all of the areas are also variable; however, in areas with a significant amount of data (areas 3, 4 and 5) a radial pattern can be seen where lineations point from north and south towards the east and west directions, representing the relative movement of the footwall to the hanging wall (Fig. 4.16). In all five areas, the intermediate seismic strain axes (the Y-axes) are sub-vertical, while the largest and smallest seismic strain axes are sub-horizontal. Furthermore, in all five areas the largest strain axis (the X-axis) is trending about E-W, and the smallest strain axis (the Z-axis) is trending about N-S (Fig. 4.17). The stress ratios for all of the areas correspond to stress ellipsoids with unequal principal stresses ($\phi \sim 0.5$), except for area 4 which has a lower value ($\phi = 0.2$) (Fig. 4.17). All of the areas have stress ratios that define stress ellipsoids with unequal principal stresses (Fig. 3.4 (b) and (e)); however area 2 is more similar to the conditions of uniaxial compression (Fig. 3.4 (c) and (f)).

Although the results from the strike slip regime are more varied, there are consistent trends that can be seen in the reconstruction of the stress and strain ellipsoids across all five areas (Table 4.3). For instance, the horizontal strain axis trends roughly E-W in all five areas, and there is a horizontal compressive stress that is oriented about N-S.
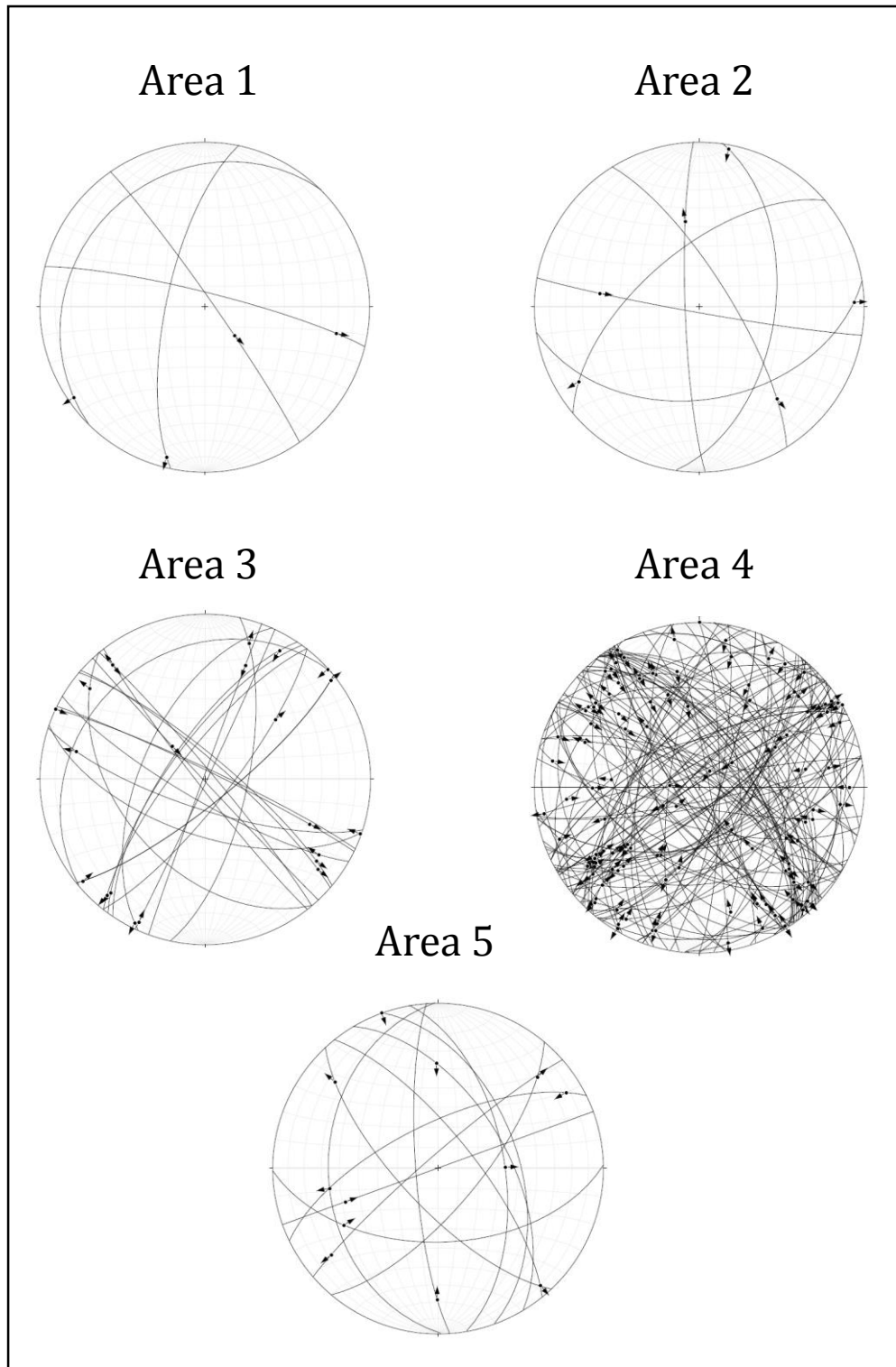
Figure 4.13: Nodal planes and the direction of slip for all seismic events of the strike slip fault regime from areas 1-5. Nodal planes are represented as great circles and the corresponding direction of slip of the hanging wall relative to the footwall is represented as the arrow attached to the great circle. The nodal planes for all strike slip events are generally steeply dipping. In all five areas, the nodal planes are commonly oriented in the NW-SE and NE-SW directions, particularly in areas 3 and 4.
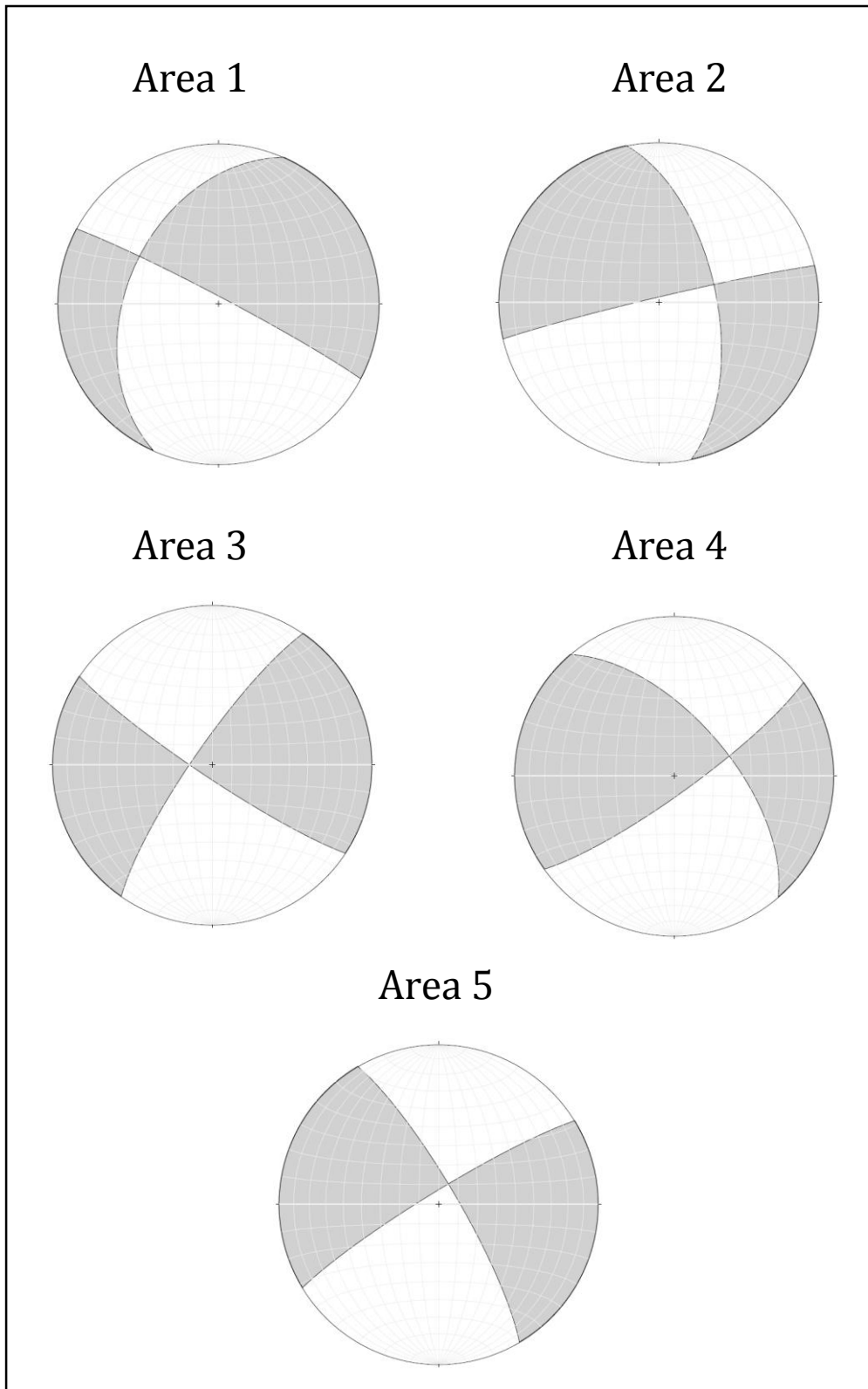
Figure 4.14: Fault plane solutions for all seismic events of the strike-slip fault regime in areas 1-5. Best-fit nodal planes are represented by great circles, shaded areas represent the tensile (T-) fields, and non-shaded areas represent the compressive (P-) fields. In all five areas, the best-fit nodal planes show a general NW-SE and NE-SW trend.
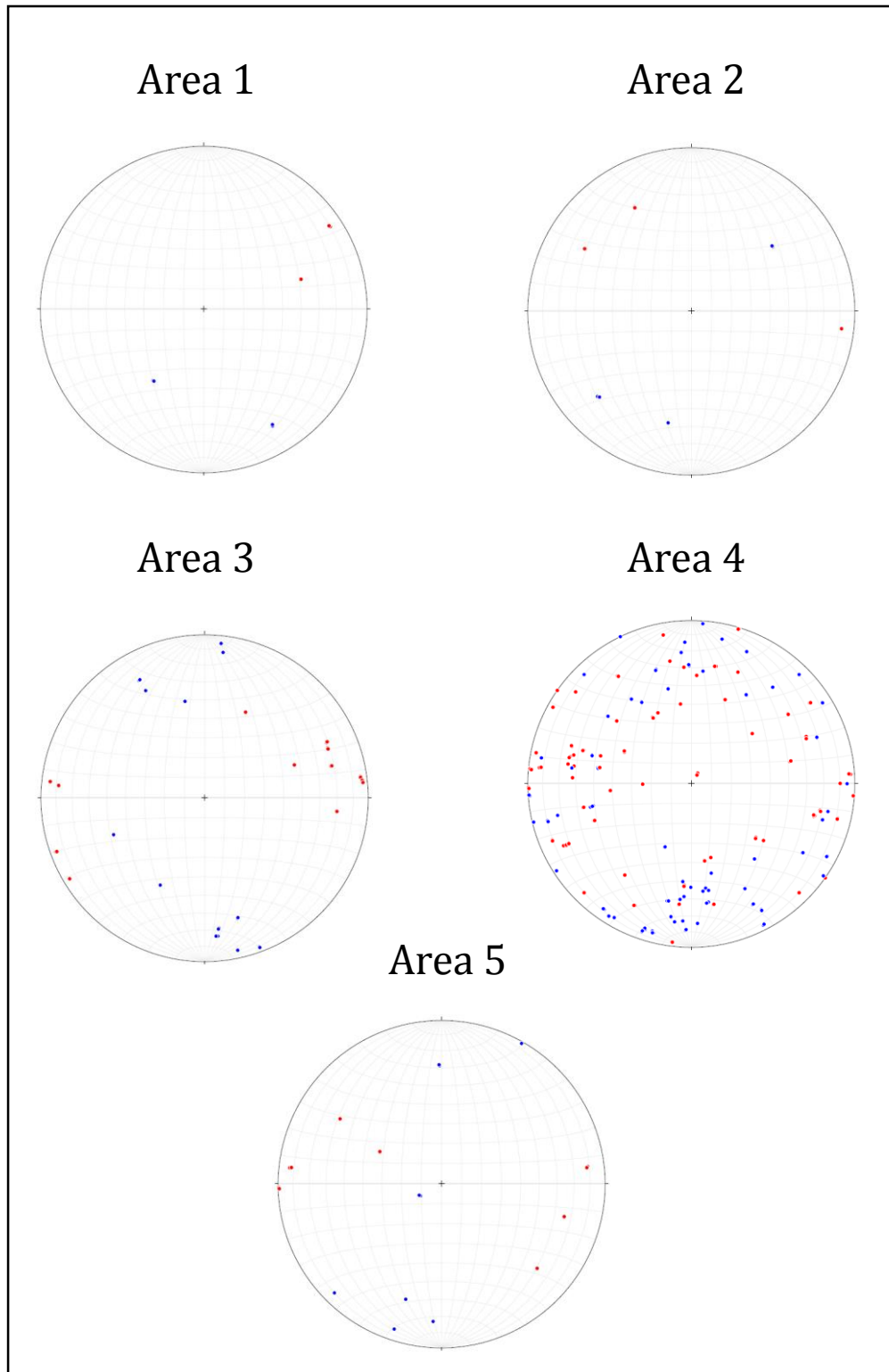
Figure 4.15: Compressive (P-) and tensile (T-) axes of all seismic events of the strike-slip fault regime in areas 1-5. T-axes are represented by red dots and P-axes are represented by blue dots. In general, the axes are clustered into four groups (two for the P-axes, and two for the T-axes) that correspond to the P- and T-sectors defined by the best-fit nodal planes in the fault plane solutions; however, area 5 illustrates highly variable orientations of the P- and T-axes.
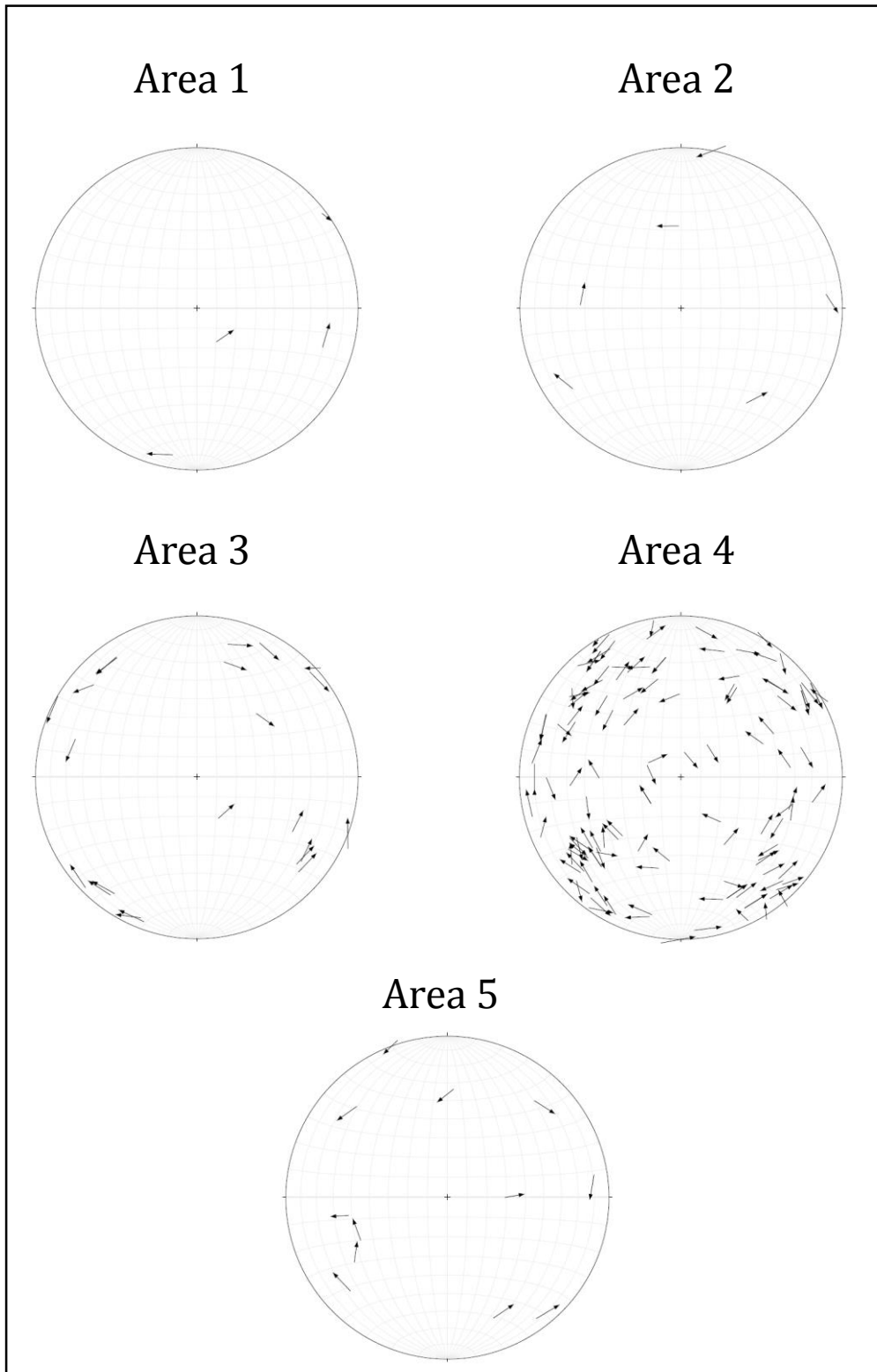
Figure 4.16: Tangent lineations for all seismic events of the normal fault regime in areas 1-5. The directions of the arrows correspond to the movement of the footwall relative the hanging wall. Although it is difficult to see trends in areas with very little data (areas 1 and 2), it can be seen that there is a radial pattern of the lineations pointing from north and south towards east and west.
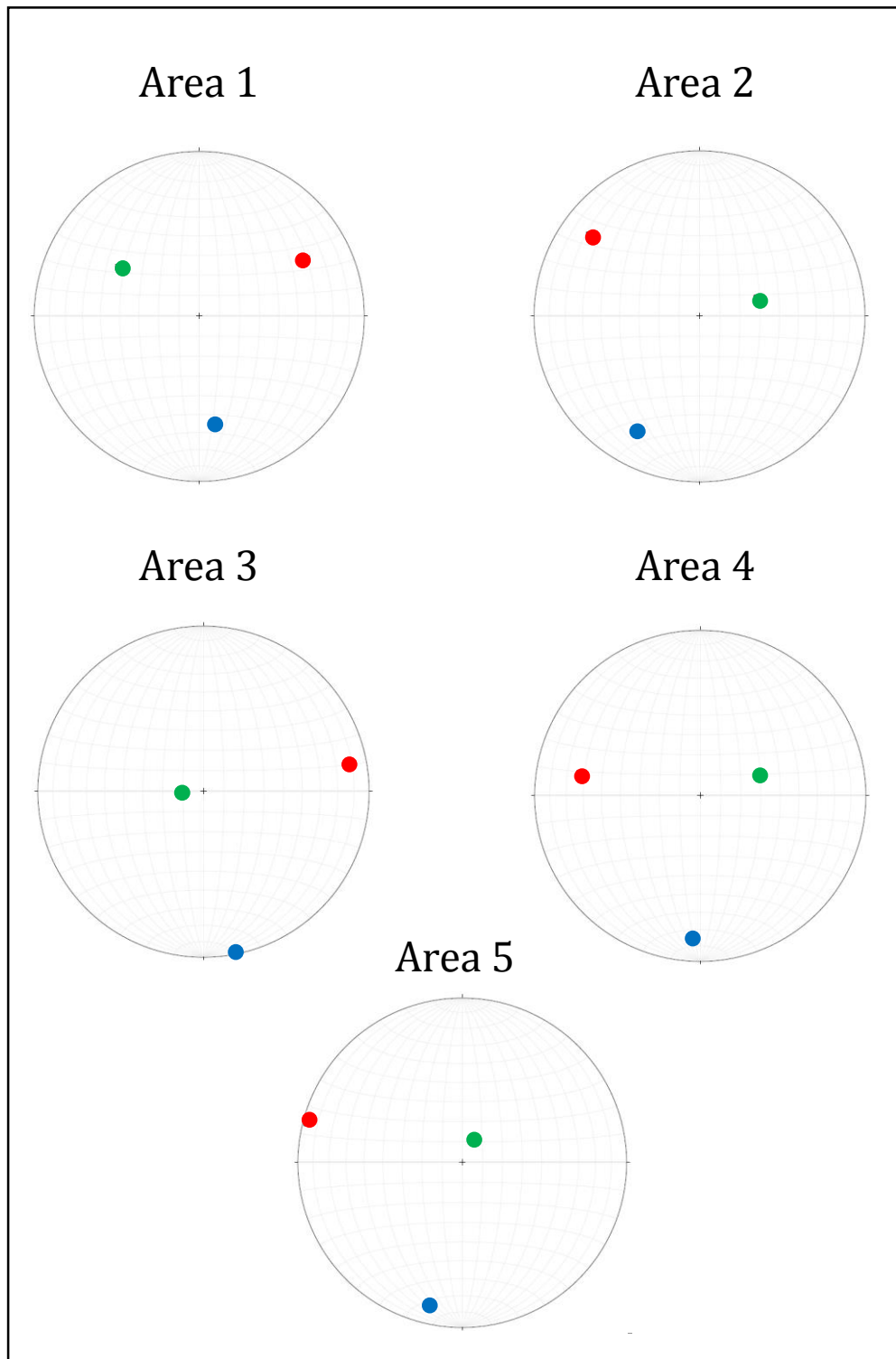
Figure 4.17: Kinematic axes depicting the orientations of the axes of the strain ellipsoid for all seismic events of the strike slip fault regime in areas 1-5. The largest strain axis (the X-axis) is represented by the red circle, the smallest strain axis (the Z-axis) is represented by the blue circle, and the intermediate strain axis (the Y-axis) is represented by the green circle. In all three areas the Y-strain axis is close to vertical, while the X-strain axis changes from NE-SW orientation in the western regions to E-W orientation in the eastern regions. The Z-strain axis does not vary in orientation much from the N-S direction, however it is dipping slightly more steeply in areas 1 and 2.
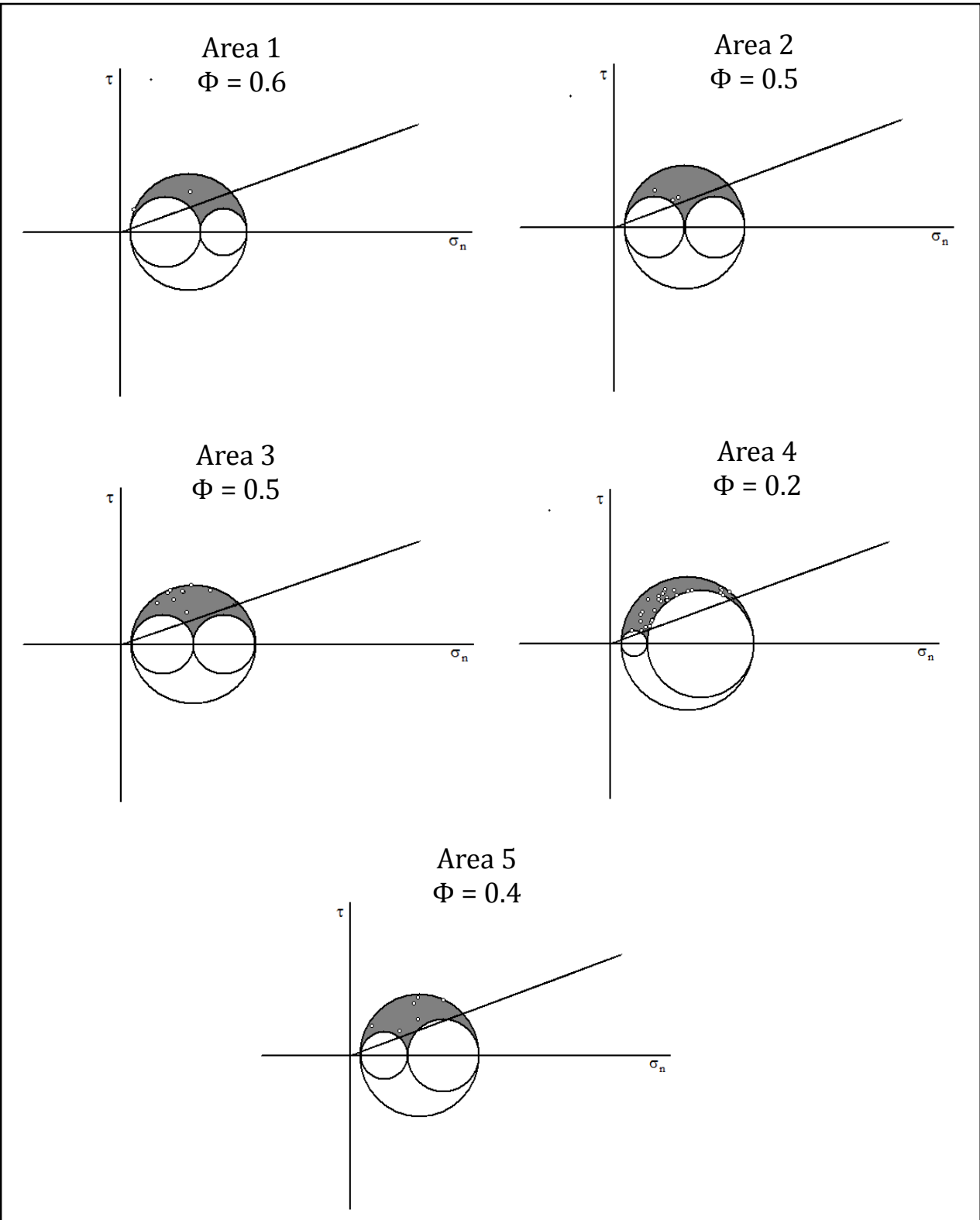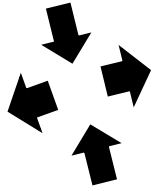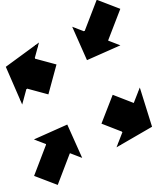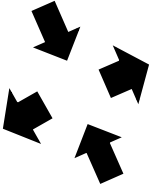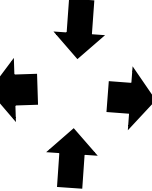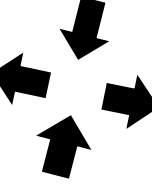
Figure 4.18: The stress ratio values (Φ) and corresponding dimensionless Mohr diagrams for the strike slip fault regime in areas 1-5. Areas 1, 2, 3, and 5 have a stress ratio values near Φ = 0.5 which corresponds to a stress ellipsoid defined by unequal principal stresses (Fig. 3.4 (b) and (e)). Area 2 has a lower stress ratio that corresponds more closely to a stress ellipsoid defined by uniaxial compression (Fig. 3.4 (c) and (f)).

Table 4.3: A summary of the key stress and strain characteristics of the strike slip faulting events for areas 1-5. The orientations of the nodal planes do not change drastically from west to east along the Orogen. The horizontal strain axes are also relatively similar in all areas in that the compressive axis trends roughly N-S and the extensional axis trends roughly E-W.

		Area 1	Area 2	Area 3	Area 4	Area 5
Strike Slip Fault Regime	Best-Fit Nodal Plane Orientations	NW-SE and NNE-SSW	NNW-SSE and ENE-WSW	NW-SE and NE-SW	NW-SE and NE-SW	NW-SE and NE-SW
	Stress Ratio Value	$\Phi = 0.6$	$\phi = 0.5$	$\Phi = 0.5$	$\phi = 0.2$	$\phi = 0.4$
	Horizontal Strain Axis Orientations					

5.0 Discussion

5.1 Crustal Stress Regimes

Applying both fault slip inversion and kinematic analysis to the seismic data for each geographical area of this study has shown that there are three well-defined fault regimes present throughout the Himalayan seismic belt and the area immediately north in the Tibetan Plateau – the normal fault regime, the thrust fault regime, and the strike slip fault regime. It is also apparent that the Shillong Plateau region (area 5) is dominated by solely strike slip faulting events. Based on the geographical locations of the epicenters of the seismic events (Fig. 5.1) it is possible to deduce the likely stress fields that have contributed to a large majority of the seismicity in the Himalayas since 1977. From this information it is then possible to make inferences about the cause behind the seismic gap in
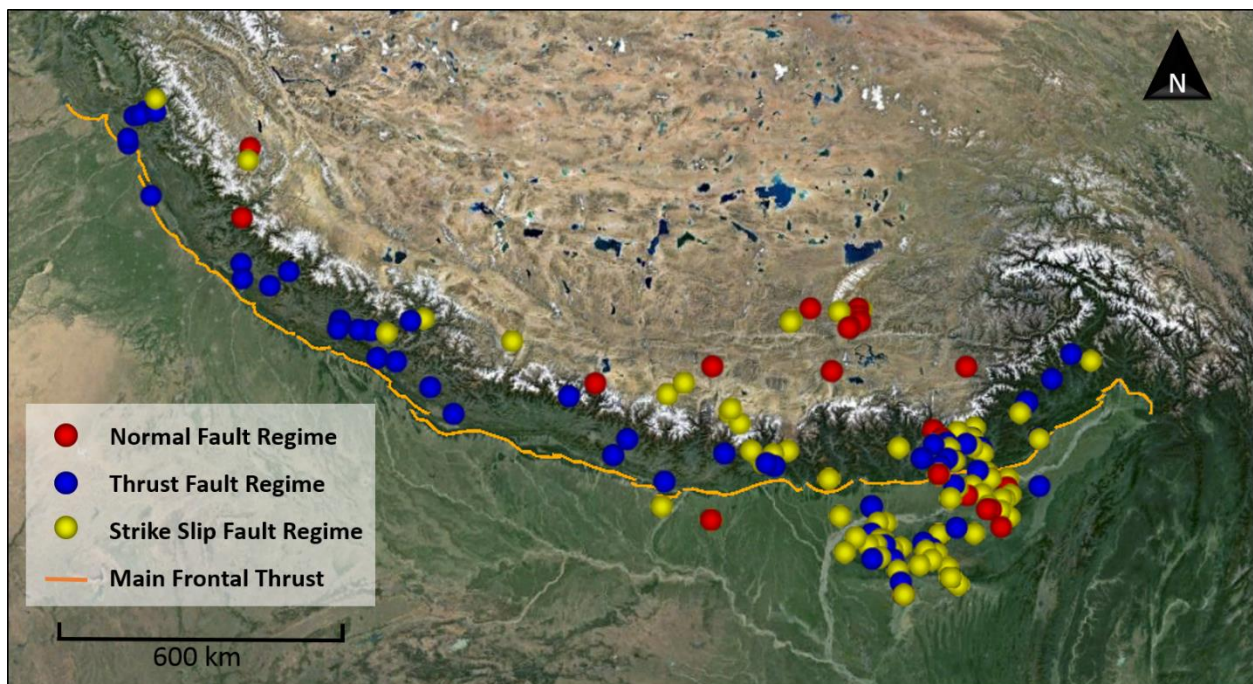
Figure 5.1: Epicenters of earthquakes for seismic events (M > 4) from the ANSS catalogue from 1977-2014. Thrust faults (blue) follow the curvature of the arc and are located in the seismic belt. Strike Slip faults (yellow) are located mainly in the seismic belt of the eastern Himalayas and to the south in the Shillong Plateau region. Normal faults (red) are located at the southern margin of the Tibetan Plateau. (Map data: Google, Mapabc.com).

the Bhutan Himalaya despite the increased convergence rates of India and Eurasia in the eastern regions of the Orogen relative to the western regions.

5.1.1 Normal Fault Regime

The majority of normal faulting events are located along the southern margin of the Tibetan Plateau (Fig. 5.1). The crustal stress analyses for this regime show consistent E-W extension that does not vary with the curvature of the arc. For these reasons, the majority of the normal fault seismicity is interpreted to be related to movement along the normal faults of the South Tibetan Grabens (Fig. 2.3). Therefore, the normal faulting regime is interpreted to be associated with seismic strain conditions that are distinctly different than the seismic strain conditions acting on the Himalayas. It is important to note that many of the normal faults of the South Tibetan Grabens do not fall within the geographical areas used in this study (Fig. 1.2). This makes the results for seismic events of the normal faulting regime biased; however, the processes that contribute to the formation of the South Tibetan Grabens are outside the scope of this study, so the normal fault regime will not be discussed in further detail.

5.1.2 Thrust Fault Regime

The fault plane solutions from the thrust fault regime consistently showed two clusters of nodal planes – one that dipped steeply towards the south, and another that dipped shallowly towards the north (Fig. 4.6). The Main Himalayan Thrust (MHT), and the series of forward propagating thrust faults within the active orogenic wedge of the Himalaya are shallowly dipping towards the north (Avouac, 2003). Therefore, the nodal planes that dip shallowly northward have been interpreted as the actual fault planes.

The epicenters of the thrust faulting events generally follow the seismic belt from west to east along the Orogen (about 100 km north of the surface trace of the MFT) (Fig. 5.1). The hypocenters of the thrust fault seismicity are averaged at a depth of 21 km ± 5 km. At a distance of 100 km north of the surface trace of the Main Frontal Thrust (MFT), the Main Himalayan Thrust (MHT) is at a depth of ~15-20 km (Ader *et al.*, 2012). Therefore, the majority of thrusting events contributing to the seismic belt of the Himalayas are interpreted to be the result of slip along the MHT.

5.1.3 Strike Slip Fault Regime

The frequency of strike slip faulting events increases dramatically in the eastern regions of the Himalayas (areas 3 and 4) (Fig. 5.1) which is congruent with the strike slip faults that have been documented in the Bhutan Himalayan region (De & Kayal, 2003; De & Kayal, 2004; Drukpa *et al.,* 2006). This increase in strike-slip faulting events correlates to the increase in plate convergence rate by 10 mm/year in the north-eastern section of the collision zone relative to the north-western section (Molnar & Stock, 2009). Therefore, as a part of this study, it is hypothesized that the increase in strike slip faulting events in the east accommodates for the increased plate convergence rate in this area.

5.2 Seismic Energy and Slip Rates

Calculations were performed on both the thrust and strike-slip seismic data to test the theory that the increased rate of convergence in the north-eastern section of the Himalayas is accommodated by slip occurring along transverse faults in the Indian crust. For each of the five areas, the total displacement that occurred along both thrust and strike slip faults, as well as the total amount of energy released from each, was calculated. These results were then compared between the thrust and strike slip events to determine how

they change along strike of the orogen. The amount of change was then compared to the eastward increase in north-south plate convergence rates (Molnar & Stock, 2009) to establish any correlations between the two.

5.2.1 Total Energy Released

The amount of energy released from each seismic event was calculated based on the seismic moment (M_o), which is a measurement of the amount of energy released by a faulting event (eq. 2). Most of the events from the ANSS catalogue had recorded body-wave magnitudes (m_b). Other events, such as the focal mechanisms obtained from Baruah *et al.* (2013), had recorded surface-wave magnitudes (M_s). The M_s values were converted to m_b values via the following equation:

$$m_b = (0.46 \text{ X M}_s) + 2.74 \qquad \text{(eq. 3)}$$

(Scordilis, 2006).

For the events that were not provided in the ANSS catalogue, seismic moment (Mo) values were calculated via the following equation:

$$\log(M_o) = 2.00 m_b + 13.75 \qquad \text{(eq. 4)}$$

(Chen *et al.*, 2007 and references therein).

The M_o values for thrust and strike slip events were summed for each of the five areas (Table 5.1). A comparison between the different fault regimes along strike of the Orogen show a general increase in the amount of energy released from west to east along the Himalayas (areas 1-4), with an anomalously high value for the strike slip events in area 3 (Fig. 5.2) where there were several high-magnitude (>6 M_o) seismic events since 1977.

Table 5.1: Total amount of energy released on thrust and strike slip faults in areas 1-5 from 1977 – 2014. These totals were calculated using equations 3 and 4 and by summing M_o values for each area.

Area	Longitude	Thrust Faults		Strike Slip Faults	
		Total Energy Released (Joules)	Error (+/- Joules)	Total Energy Released (Joules)	Error (+/- Joules)
1	**74.0-80.0**	7.7 E+16	2.3 E+15	1.7 E+17	5.1 E+15
2	**80.0-86.0**	1.0 E+19	8.3 E+17	3.8 E+17	1.1 E+16
3	**86.0-89.0**	2.4 E+18	1.9 E+17	5.7 E+19	4.6 E+18
4	**87.5-93.0**	1.2 E+19	9.4 E+17	7.8 E+18	6.2 E+17
5	**89.0-95.5**	0	0	6.0 E+17	1.8 E+16
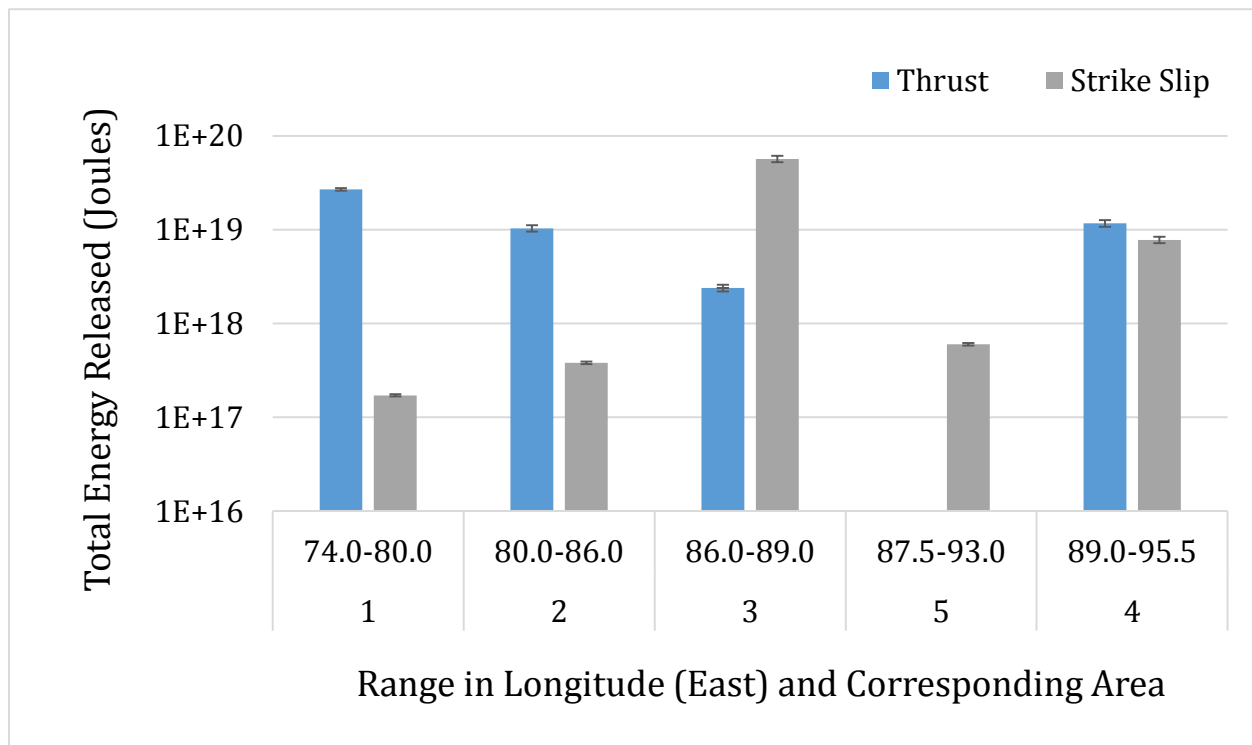
Figure 5.2: Total energy released on thrust faults (blue) and strike slip faults (gray) in areas 1-5 from 1977-2014. Note that the strike slip faults in area 3 released the largest amount of seismic energy according to the M_o values, despite covering the smallest range in longitude.

The total amount of energy released on the faults shows a general increase from west to east along the Orogen (areas 1-4 respectively), with the exception of area 3 being the highest. This increase in seismic energy shows similar trends to the increase in seismic activity in the eastern Himalayas (illustrated by the amount of data shown in the nodal plane diagrams for each fault regime (Figs. 4.1, 4.7, and 4.13)). For these reasons, the eastward increase in seismicity rate can be correlated to the 10 mm/year eastward increase in convergence rate (Molnar & Stock, 2009).

5.2.2 Total Slip and Slip Rates

The total amount of slip released by each fault was calculated as an additional means to determine whether the increased number of strike slip events in the eastern Himalayas accounts for the increased rate of northward convergence of the Indian plate. The amount of slip was calculated from the moment magnitude (M_w). The M_w values were recorded for events from the ANSS catalogue but had to be calculated for the events from Baruah *et al.* (2013) from the m_b value. The following equation was used to calculate the M_w value:

$$M_w = 0.85m_b + 1.03 \qquad \text{(eq. 5)}$$

(Scordilis, 2006).

Once the M_w values were obtained for all seismic events of the thrust fault and strike slip regimes, the following equation was used to calculate the area (A) on which the slip occurred:

$$M_w = \log A + 4.03 \qquad \text{(eq. 6)}$$

(Hanks & Bakun, 2014).

The seismic moment (M_o), the area (A), and the shear modulus (μ), were used to calculate total slip that occurred on each event (D). For the shear modulus (μ), a value of 40 GPa was used (Bettinelli *et al.,* 2008). The following equation was rearranged to calculate the total slip:

$$M_o = \mu A D \qquad \text{(Same as eq. 2)}$$

The slip values (D) were summed for each area for both the thrust and strike slip events. To get the slip rate, the total slip values were divided by the number of years this study covers (38 years) (Tables 5.2 and 5.3). A comparison between the different fault regimes along strike of the Orogen showed larger amounts of slip in the eastern regions (areas 3 and 4) than in the western regions (areas 1 and 2) (Figure 5.3 and 5.4). It is also notable that strike slip faults are dominant in the eastern Himalayas (areas 3 and 4).

Table 5.2: Total slip (in mm) that has occurred along thrust faults in all five areas, as well as the corresponding slip rate (in mm/year).

Area	Longitude	Thrust Faults			
		Total Slip (mm)	Error (+/- mm)	Slip Rate (mm/year)	Error (+/- mm/year)
1	**74.0-80.0**	126	16	3	0.50
2	**80.0-86.0**	2583	465	68	14
3	**86.0-89.0**	991	178	26	5
4	**87.5-93.0**	4299	774	113	23
5	**89.0-95.5**	0	0	0	0

Table 5.3: Total slip (in mm) that has occurred along strike slip faults in all five areas, as well as the corresponding slip rate (in mm/year).

Area	Longitude	Strike Slip Faults			
		Total Slip (mm)	Error (+/- mm)	Slip Rate (mm/year)	Error (+/- mm/year)
1	**74.0-80.0**	290	38	8	1
2	**80.0-86.0**	390	51	10	2
3	**86.0-89.0**	3575	643	94	19
4	**87.5-93.0**	4744	854	125	25
5	**89.0-95.5**	832	108	22	3
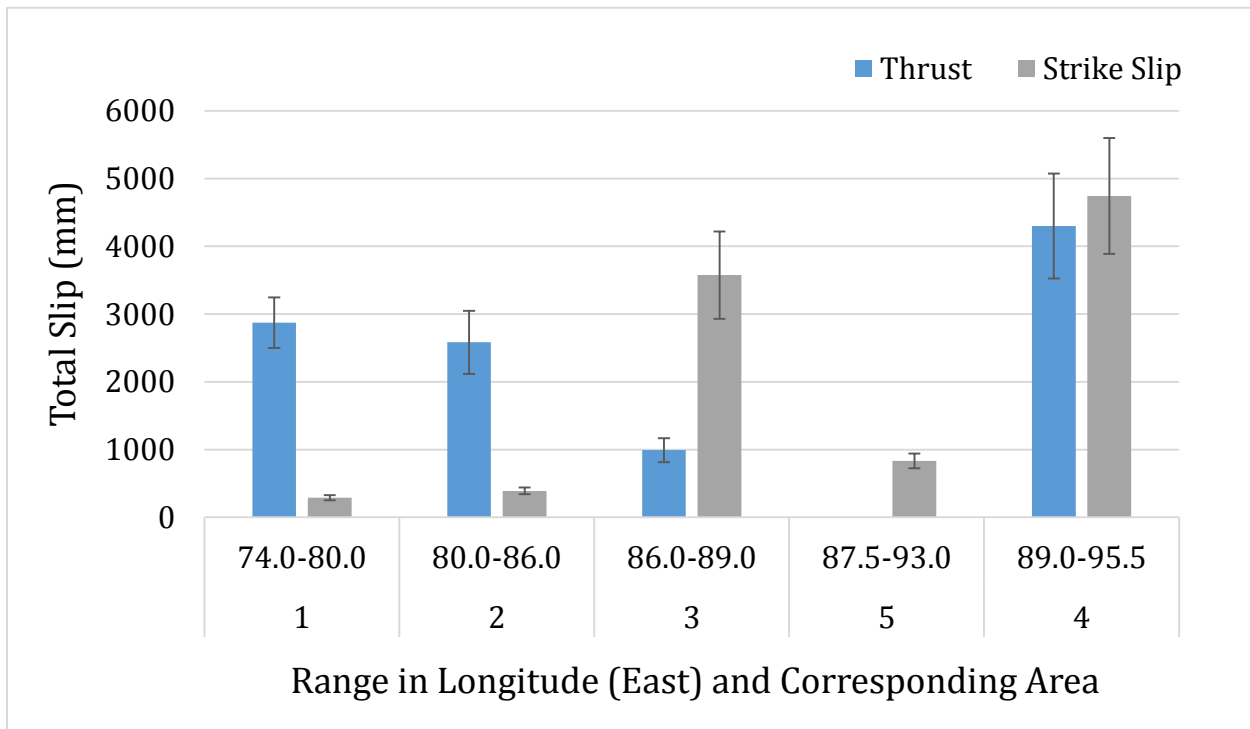
Figure 5.3: Total slip that occurred from thrusting events (blue) and strike slip events (gray) in areas 1-5 from 1977-2014. Note that slip along thrust faults dominates in the western regions (areas 1 and 2) and slip along strike slip faults dominates in the eastern regions (areas 3 and 4).
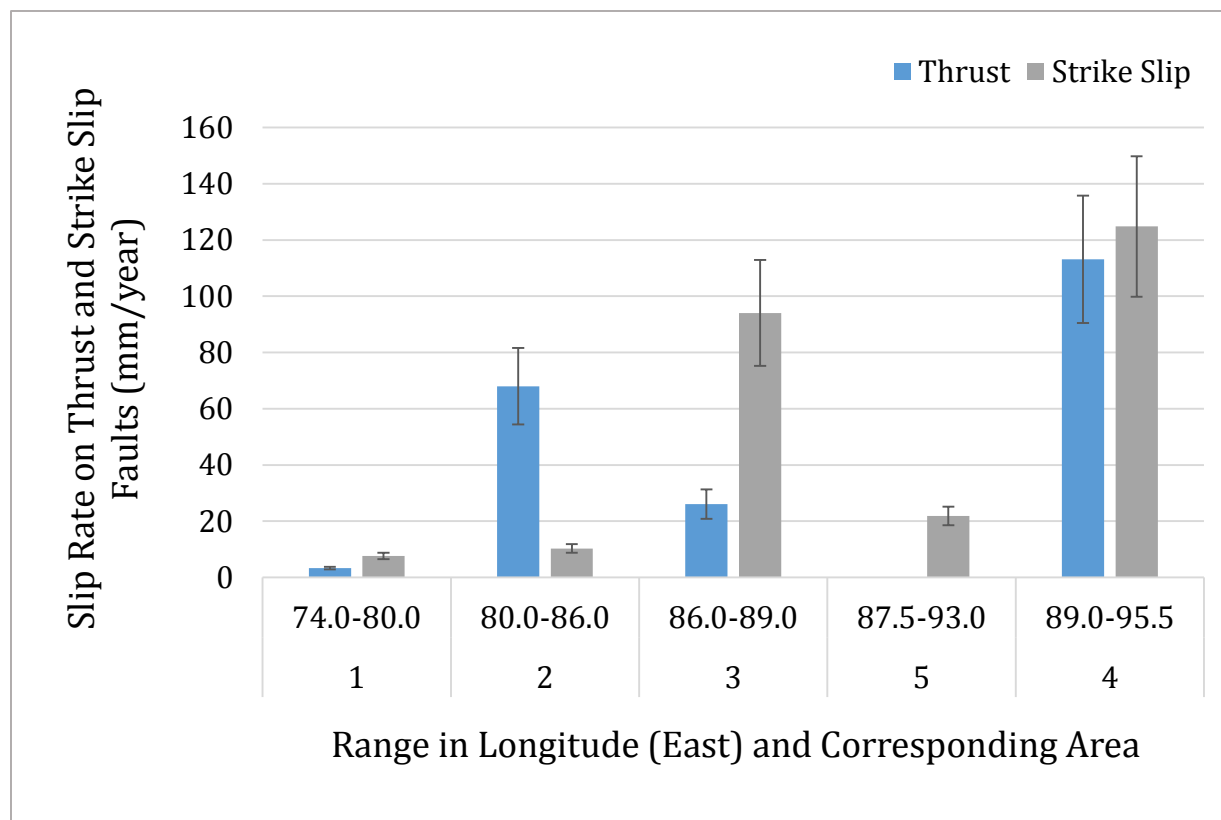
Figure 5.4: Slip rates from thrusting events (blue) and strike slip events (gray) in areas 1-5 from 1977-2014. Note that slip rates on strike slip faults are larger than on thrust faults in the eastern regions (areas 3 and 4), but not in the western regions (areas 1 and 2).

These calculations show that there is an eastward-increasing amount of slip occurring along both thrust and strike slip faults that is likely associated with the eastward-increasing seismicity rates and seismic energy release. Furthermore, the total amount of slip calculated for thrust and strike slip faults showed a notable change from area 2 to area 3. In the western Himalayas (areas 1 and 2) the thrust fault regime accounted for the majority of slip, while in the eastern Himalayas (areas 3 and 4) the strike slip regime accounted for the majority of slip. This observation supports the hypothesis that the abundance of strike slip faulting events in the east have helped accommodate the increased plate convergence rates in this region.

5.3 Strain Partitioning

From the slip and seismic energy calculations it is evident that thrust faulting events dominate in the west, and strike slip faulting events dominate in the east; however, the amount of slip and energy released on thrust faults in the eastern regions, particularly area 4, is still significant (Figs. 5.2 and 5.3). It is therefore apparent that the eastern regions of the Himalayas are experiencing a strong component of strain partitioning between both thrusting and strike slip seismic strain conditions.

The strike slip faults in the eastern Himalaya predominantly trend N-S and have a dextral sense of slip. A probable cause for slip occurring along these right-lateral strike slip faults in the eastern Himalaya is rotation of the Indian subcontinent. Recent studies have suggested that portions of the north-east Indian crust are rotating clockwise relative to India (Clark & Bilham, 2008; Vernant *et al.*, 2014). This rotational motion combined with the northward convergence of India into Eurasia, may be the cause behind the strain partitioning between a N-S component of compression (resulting in thrusting along the MHT) and an E-W component of extension (from oblique movement along N-S trending, right-lateral strike slip faults).

Another important thing to note about the strike slip seismic events of the eastern Himalaya is that the nodal plane orientations showed conjugate fault sets (Fig. 4.13). Conjugate fault sets can take up north-south convergence by simultaneous movement along both transverse faults. Therefore, these strike slip faults can be activated from the N-S compression that is evident in the thrust fault regime as well.

6.0 Conclusions

Based on the analyses of the seismic strain and stress in the crust of the Himalayas, the seismotectonics of the region can be separated into three main fault regimes: the normal fault regime, the thrust fault regime, and the strike slip fault regime. The normal fault regime is associated with the E-W extension occurring in the Tibetan Plateau along the South Tibetan Grabens. Its unwavering paleostress and strain axes from west to east along the Orogen suggest that the seismic strain associated with this regime is distinctly different than the seismic strain causing the seismicity in the rest of the Himalayas. Furthermore, both the thrust and strike slip fault regimes appear to be associated with similar seismic strain conditions, as their paleo-stress and strain axes have similar orientations, and the conjugate strike slip fault sets can accommodate N-S shortening.

The calculations performed on the quantity of energy produced by rupturing, as well as the amount of slip occurring along thrust and strike slip faults, show that the thrust fault regime dominates the western Himalayan regions, while the strike slip regime dominates the eastern Himalayan regions. As a part of this study, it is suggested that the increase in strike slip seismic events in the east accommodates for the 10 mm/year increased convergence rate in this region (Molnar & Stock, 2009). This result is significant as it could suggest that strain is not accumulating as drastically on the locked portion of the MHT in the eastern Himalaya as previously theorized (Bilham *et al.*, 2001); rather it is being released along conjugate sets of transverse faults in the Indian crust.

Given these energy and slip values, there is also unmistakeable strain partitioning occurring in the eastern Himalayas (area 4) between thrusting and strike slip seismic strain conditions. Recent studies show that portions of the north-eastern Indian crust exhibit

clockwise rotation relative to India (Clark & Bilham, 2008; Vernant *et al.*, 2014). As a part of this study it is suggested that the strain partitioning in the eastern Himalaya is the result of both the northward convergence of the Indian plate, as well as the clockwise rotation of a portion of the north-eastern Indian crust.

6.1 Recommendations for Future Research

In order to further our understanding of the distribution of seismic strain and stress in the crust of the Himalayas, it is first important to find a direct cause for the seismic gap in the Bhutan Himalayan region. This study provides insight as to how the strike slip nature of the eastern Himalaya is related to the crustal stress regimes of the Himalayan Orogen. It also suggests that stress that was theorized to be accumulating along a locked portion of the MHT may actually be being released along strike slip faults in the Indian crust; however, the cause for the existence of an area of low seismicity in the midst of this strike slip dominated area remains puzzling. A similar, but more in-depth, analysis of the crustal stress distributions in solely the eastern Himalaya should be conducted in order to gain further insight. Furthermore, it is possible that focusing a similar type of study on the microseismicity in this region could reveal a more detailed and accurate account of the seismic energy and fault slip distribution along crustal faults of the Himalaya.

7.0 References

Allmendinger, R.W., Cardozo, N.C., and Fisher, D. (2012). Structural Geology Algorithms: Vectors & Tensors: Cambridge, England, Cambridge University Press, 289 pp.

Angelier, J. (1984) Tectonic analysis of fault slip data sets. *Journal of Geophysical Research, 89.* 5835–5848.

Armijo, R., Tapponnier, P., Mercier, J. L. & Han, T. (1986). Quaternary extension in southern Tibet: field observations and tectonic implications. *Journal of Geophysical Research, 91.* 13 803–13 872

Banerjee, P., Burgmann, R., Nagarajan, B., Apel, E. (2008). Intraplate deformation of the Indian subcontinent. *Geophysical Research Letters, 35.* doi: 10.1029/2008GL035468

Baruah, S., Baruah, S., Kayal, J.R. (2013). State of tectonic stress in northeast India and Adjoining South Asia Region: An Appraisal. *Bulletin of the Seismological Society of America, 103,* 894-910. doi: 10.1785/0120110354

Bettinelli, P., Avouac, J., Flouzat, M., Bollinger, L., Ramillien, G., Rajaure, S., Sapkota. S. (2008). Seasonal variations of seismicity and geodetic strain in the Himalaya induced by surface hydrology. *Earth and Planetary Science Letters, 266*(3), 332-344.

Bilham, R. & Ambraseys, N. (2005). Apparent Himalayan Slip Deficit from the Summation of Seismic Moments for Himalayan Earthquakes, 1500-2000. *Current Science, 88*(10), 1658-1663.

Bilham, R. & England, P. (2001). Plateau 'pop-up' in the great 1897 Assam earthquake. *Nature, 410*, 806-808.

Bilham, R., Gaur, V.K., Molnar, P. (2001). Himalayan Seismic Hazard. *Science, 293,* 1442-1444.

Biswas, S., I. Coutand, D. Grujic, C. Hager, D. Stöckli, and B. Grasemann (2007). Exhumation and uplift of the Shillong plateau and its influence on the eastern Himalayas: New constraints from apatite and zircon (U-Th-[Sm])/He and apatite fission track analyses. *Tectonics, 26.* TC6013. doi:10.1029/ 2007TC002125

Blisniuk, P.M., Hacker, B.R., Glodny, J., Ratschbacher, L., Bi, S., Wu, Z....Calver, A. (2001). Normal faulting in central Tibet since at least 13.5 Myr ago. *Nature, 412,* 628-632.

Clark, M. K., & R. Bilham (2008). Miocene rise of the Shillong Plateau and the beginning of the end for the Eastern Himalaya. *Earth Planet. Sci. Lett., 269.* 337–351, doi:10.1016/j.epsl.2008.01.045

De, R., & Kayal, J. R. (2003). Seismotectonic model of the Sikkim Himalaya: Constraint from microearthquake surveys. *Bulletin of the Seismological Society of America*, *93*(3), 1395-1400.

De, R., & Kayal, J. R. (2004). Seismic activity at the MCT in Sikkim Himalaya. *Tectonophysics*, *386*(3), 243-248.

DeMets, C., Gordon, R.G., Argus, D. F., Stein, S. (1994). Effect of recent revisions to the geomagnetic reversal time scale on estimates of current plate motions. *Geophysical Research Letters, 21*(20). 2191-2194.

Drukpa, D., Velasco, A. A., & Doser, D. I. (2006). Seismicity in the Kingdom of Bhutan (1937–2003): Evidence for crustal transcurrent deformation. *Journal of Geophysical Research: Solid Earth (1978–2012)*, *111*(B6).

Dziewonski, A. M., T.-A. Chou and J. H. Woodhouse, Determination of earthquake source

    parameters from waveform data for studies of global and regional seismicity, J.

    Geophys. Res., 86, 2825-2852, 1981. doi:10.1029/JB086iB04p02825

Ekström, G., M. Nettles, and A. M. Dziewonski, The global CMT project 2004-2010: Centroid-

    moment tensors for 13,017 earthquakes, Phys. Earth Planet. Inter., 200-201, 1-9,

    2012. doi:10.1016/j.pepi.2012.04.002

Faultkin 7 (Version 7.2.9) [Computer software]. Allmendinger. Retrieved from:

    http://www.geo.cornell.edu/geology/faculty/RWA/programs/faultkin.html

Fossen, H. (2010). Structural Geology. New York, New York: Cambridge University Press

Gahalaut, V.K., Rajput, S., Kundu, B. (2011). Low Seismicity in the Bhutan Himalaya and the

    Stress Shadow of the 1897 Shillong Plateau Earthquake. *Physics of the Earth and*

    Planetary Interiors, 186, 97-102. doi: 10.1016/j.pepi.2011.04.009

Hanks, T.C., & Bakun, W.H. (2014). M-logA Models and Other Curiosities. *Bulletin of the*

    Seismological Society of America, 104(5), 2604-2610. doi: 10.1785/0120130163

Hodges, K.V. (2000). Tectonics of the Himalaya and southern Tibet from two perspectives.

    GSA Bulletin, 112(3), 324-350. doi: 10.1130/0016-7606(2000)1122.0.CO;2

Langille, J.M., Jessup, M.J., Cottle, J., Ahmad, T. (2014). Kinematic and thermal studies of the

    Leo Pargil Dome: Implications for synconvergent extension in the NW Indian

    Himalaya. *Tectonics, 33.* doi: 10.1002/2014TC003593

Marret, R.A., and Allmendinger, R.W., 1990, Kinematic Analysis of Fault-Slip Data: Journal of

    Structural Geology, v. 12, p. 973-986.

Molnar, P. & Stock, J.M. (2009). Slowing of India's convergence with Eurasia since 20 Ma

    and its implications for Tibetan mantle dynamics. *Tectonics, 28*, 1-11. doi:

    10.1029/2008TC002271

Patriat, P., & Achache, J. (1984). India-Eurasia collision chronology has implications for

    crustal shortening and driving mechanism of plates. *Nature, 311,* 615-621.

Ratschbacher, L., Krumrei, I., Blumenwitz, M. (2011). Rifting and strike-slip shear in central

    Tibet and the geometry, age and kinematics of upper crustal extension in Tibet.

    Geological Society, London, Special Publications, 353, 127-163. doi: 10.1144/SP353.8

Scordilis, E.M. (2006). Empirical global relations converting Ms and mb to moment

    magnitude. *Journal of Seismology, 10,* 225-236. doi: 10.1007/s10950-006-9012-4

T-Tecto (Version 3.0) [Computer Software]. Slovenia: Jure Zalohar. Retrieved from:

    http://www2.arnes.si/~jzaloh/download_t-tecto.htm

U.S. Geological Survey. (2012). Earthquake glossary- earthquake hazard*.* Retrieved 11/20,

    2014 from: http://earthquake.usgs.gov/learn/glossary/

Vernant, P., Bilham, R., Szeliga, W., Drukpa, D., Kalita, S., Bhattacharyya...Berthet, T. (2014).

    Clockwise rotation of the Brahmaputra Valley relative to India: Tectonic

    convergence in the eastern Himalaya, Naga Hills, and Shillong Plateau. *Geophysical*

    Research. Solid Earth, 119, 6558-6571. doi: 10.1002/2014JB011196

Zalohar, J., Vabrec, M. (2007). Paleostress Analysis of Heterogeneous Fault-Slip Data: The

    Gauss Method. *Journal of Structural Geology, 29,* 1798-1810.

    doi:10.1016/j.jsg.2007.06.009

Zhang, P.-Z., Shen, Z., Wang, M., Gan, W., Bürgmann, R., Molnar, P..., Xinzhao, Y. (2004).

Continuous deformation of the Tibetan Plateau from global positioning system data.

Geological Society of America, 32(9), 809-812. doi: 10.1130/G20554.1

8.0 Appendix

8.1 Appendix A

*Data from Area 1:

<table>
<tr><td colspan="18" align="center">Normal</td></tr>
<tr>
<td>Event Name</td>
<td>Date</td>
<td>Time</td>
<td>Depth (CMT)</td>
<td>Lat</td>
<td>Long</td>
<td>Mw</td>
<td>mb</td>
<td>Ms</td>
<td>Mo</td>
<td>Nodal Plane 1 strike</td>
<td>Nodal Plane 1 dip</td>
<td>Nodal Plane 1 rake</td>
<td>Nodal Plane 2 strike</td>
<td>Nodal Plane 2 dip</td>
<td>Nodal Plane 2 rake</td>
</tr>
<tr><td>082380A</td><td>August 23, 1980</td><td>21:36:55.2</td><td>15.0</td><td>32.59</td><td>75.37</td><td>5.5</td><td>5.2</td><td>4.9</td><td>2.30E+24</td><td>293</td><td>10</td><td>063</td><td>140</td><td>81</td><td>095</td></tr>
<tr><td>082380B</td><td>August 23, 1980</td><td>21:50:05.7</td><td>15.0</td><td>32.49</td><td>75.40</td><td>5.5</td><td>5.2</td><td>4.8</td><td>2.61E+24</td><td>298</td><td>12</td><td>082</td><td>126</td><td>78</td><td>092</td></tr>
<tr><td>042686B</td><td>April 26, 1986</td><td>7:35:20.0</td><td>15.0</td><td>31.59</td><td>76.06</td><td>5.5</td><td>5.5</td><td>5.3</td><td>2.28E+24</td><td>299</td><td>19</td><td>058</td><td>153</td><td>74</td><td>100</td></tr>
<tr><td>071686B</td><td>July 16, 1986</td><td>22:03:12.4</td><td>15.0</td><td>30.48</td><td>78.19</td><td>5.4</td><td>5.6</td><td>5.1</td><td>1.66E+24</td><td>278</td><td>17</td><td>037</td><td>152</td><td>80</td><td>104</td></tr>
<tr><td>101991G</td><td>October 19, 1991</td><td>21:23:21.6</td><td>15.0</td><td>30.22</td><td>78.24</td><td>6.8</td><td>6.5</td><td>7.1</td><td>1.77E+26</td><td>317</td><td>14</td><td>115</td><td>112</td><td>84</td><td>078</td></tr>
<tr><td>032899F</td><td>March 28, 1999</td><td>19:05:18.1</td><td>15.0</td><td>30.38</td><td>79.21</td><td>6.5</td><td>6.4</td><td>6.6</td><td>7.77E+25</td><td>280</td><td>07</td><td>075</td><td>115</td><td>83</td><td>092</td></tr>
<tr><td>092801A</td><td>September 28, 2001</td><td>4:37:58.7</td><td>40.5</td><td>33.00</td><td>75.46</td><td>4.9</td><td>5.1</td><td>4.7</td><td>2.63E+23</td><td>323</td><td>32</td><td>105</td><td>125</td><td>59</td><td>081</td></tr>
<tr><td>200512140709A</td><td>December 14, 2005</td><td>7:09:54.9</td><td>34.2</td><td>30.12</td><td>78.83</td><td>5.1</td><td>5.3</td><td>0.0</td><td>5.69E+23</td><td>293</td><td>23</td><td>086</td><td>117</td><td>67</td><td>092</td></tr>
<tr><td>201305010657A</td><td>May 1, 2013</td><td>6:57:17.9</td><td>20.1</td><td>33.02</td><td>75.60</td><td>5.6</td><td>5.6</td><td>5.7</td><td>3.38E+24</td><td>328</td><td>23</td><td>113</td><td>124</td><td>69</td><td>081</td></tr>
<tr><td>201308020232A</td><td>August 2, 2013</td><td>2:32:49.7</td><td>22.1</td><td>33.09</td><td>75.95</td><td>5.1</td><td>5.4</td><td>0.0</td><td>6.21E+23</td><td>327</td><td>42</td><td>122</td><td>106</td><td>55</td><td>064</td></tr>
<tr><td>201308022137A</td><td>August 2, 2013</td><td>21:37:45.1</td><td>25.9</td><td>33.10</td><td>75.71</td><td>5.1</td><td>5.2</td><td>0.0</td><td>5.01E+23</td><td>319</td><td>28</td><td>124</td><td>101</td><td>67</td><td>073</td></tr>
<tr><td colspan="18" align="center">Thrust</td></tr>
<tr>
<td>Event Name</td>
<td>Date</td>
<td>Time</td>
<td>Depth (CMT)</td>
<td>Lat</td>
<td>Long</td>
<td>Mw</td>
<td>mb</td>
<td>Ms</td>
<td>Mo</td>
<td>Nodal Plane 1 strike</td>
<td>Nodal Plane 1 dip</td>
<td>Nodal Plane 1 rake</td>
<td>Nodal Plane 2 strike</td>
<td>Nodal Plane 2 dip</td>
<td>Nodal Plane 2 rake</td>
</tr>
<tr><td>021977B</td><td>February 19, 1977</td><td>6:15:27.1</td><td>10.0</td><td>31.28</td><td>78.13</td><td>5.7</td><td>5.4</td><td>0.0</td><td>4.76E+23</td><td>346</td><td>37</td><td>-118</td><td>199</td><td>58</td><td>-071</td></tr>
<tr><td>201307091349A</td><td>July 9, 2013</td><td>13:49:15.9</td><td>25.2</td><td>32.51</td><td>78.17</td><td>4.9</td><td>5.0</td><td>0.0</td><td>2.97E+23</td><td>175</td><td>33</td><td>-082</td><td>345</td><td>58</td><td>-095</td></tr>
</table>

										Strike Slip					
Event Name	Date	Time	Depth (CMT)	Lat	Long	Mw	mb	Ms	Mo	Nodal Plane 1 strike	Nodal Plane 1 dip	Nodal Plane 1 rake	Nodal Plane 2 strike	Nodal Plane 2 dip	Nodal Plane 2 rake
022783B	February 27, 1983	20:33:06.3	10.0	32.29	78.15	5.2	5.3	4.9	8.60E+23	192	71	-007	284	83	-160
012702D	January 27, 2002	22:33:43.4	28.8	33.32	75.91	5.2	4.9	0.0	8.54E+23	225	20	-011	325	86	-110

*Data from Area 2:

										Normal					
Event Name	Date	Time	Depth (CMT)	Lat	Long	Mw	mb	Ms	Mo	Nodal Plane 1 strike	Nodal Plane 1 dip	Nodal Plane 1 rake	Nodal Plane 2 strike	Nodal Plane 2 dip	Nodal Plane 2 rake
110397A	November 3, 1997	2:29:56.8	33.0	28.60	85.39	5.5	5.4	5.0	2.17E+24	021	31	-070	178	61	-102
										Thrust					
Event Name	Date	Time	Depth (CMT)	Lat	Long	Mw	mb	Ms	Mo	Nodal Plane 1 strike	Nodal Plane 1 dip	Nodal Plane 1 rake	Nodal Plane 2 strike	Nodal Plane 2 dip	Nodal Plane 2 rake
052079A	May 20, 1979	22:59:15.0	15.0	29.58	80.32	5.8	5.8	5.9	5.38E+24	274	07	079	105	83	091
072980C	July 29, 1980	12:23:15.9	10.0	28.96	81.11	5.5	5.7	5.2	2.23E+24	278	25	089	098	65	090
072980B	July 29, 1980	14:58:51.4	22.6	29.42	80.95	6.5	6.1	6.5	8.26E+25	290	21	091	108	69	089
010597A	January 5, 1997	8:47:31.6	15.0	29.43	80.29	5.5	5.6	5.3	2.45E+24	279	19	068	122	73	097
112701E	November 27, 2001	7:31:57.1	15.0	29.61	81.75	5.5	5.6	5.2	2.22E+24	257	04	063	104	87	092
112701F	November 27, 2001	8:53:59.4	15.0	28.91	81.49	5.4	5.4	5.3	1.59E+24	280	28	073	119	64	099

201007061908A	July 6, 2010	19:08:23.7	14.1	29.55	80.33	5.0	5.2	0.0	3.73E+23	318	25	140	085	74	071
201104041131A	April 4, 2011	11:31:44.3	18.8	29.43	80.71	5.4	5.6	5.4	1.56E+24	318	30	128	096	67	070
201306281140A	June 28, 2013	11:40:50.6	18.2	28.49	82.18	5.0	5.0	0.0	3.85E+23	294	26	095	109	64	088
102988A	October 29, 1988	9:11:00.8	18.0	27.39	85.73	5.2	5.4	4.8	7.54E+23	309	30	109	106	62	079
200510312147A	October 31, 2005	21:47:59.5	22.5	28.38	84.88	4.7	5.1	0.0	1.51E+23	120	42	097	291	48	084
201208231630A	October 31, 2005	16:30:22.9	28.9	28.05	82.65	5.0	5.0	0.0	3.56E+23	307	21	102	114	69	085
	19740324		33	27.66	86		5.4			97	88	90	280	2	93

Strike Slip															
Event Name	Date	Time	Depth (CMT)	Lat	Long	Mw	mb	Ms	Mo	Nodal Plane 1 strike	Nodal Plane 1 dip	Nodal Plane 1 rake	Nodal Plane 2 strake	Nodal Plane 2 dip	Nodal Plane 2 rake
200510310551A	October 31, 2005	5:51:18.6	47.0	29.39	81.28	4.7	5.0	0.0	1.45E+23	008	52	176	100	87	039
200812080859A	December 8, 2008	8:59:12.5	19.5	29.65	82.01	5.3	5.5	4.8	9.88E+23	230	62	-017	328	75	-151
080987C	August 9, 1987	21:15:10.0	34.0	29.30	83.77	5.6	5.6	4.8	2.68E+24	081	43	-010	178	83	-133

*Data from Area 3:

Normal															
Event Name	Date	Time	Depth (CMT)	Lat	Long	Mw	mb	Ms	Mo	Nodal Plane 1 strike	Nodal Plane 1 dip	Nodal Plane 1 rake	Nodal Plane 2 strike	Nodal Plane 2 dip	Nodal Plane 2 rake
032093I	March 20, 1993	14:52:10.8	15.0	28.87	87.64	6.2	5.9	6.0	2.47E+25	161	46	-121	022	52	-062
	20091107		18.8	29.31	86.28		5.5			178	43	-92	0	47	-88
	19930320		26.6	29.03	87.35		5.1			160	16	-106	357	75	-86
	19960703		33	29.92	88.19		5			175	27	-83	347	63	-94
	19980930		33	29.64	88.25		5.1			139	32	-112	345	60	-76

Event Name	Date	Time	Depth (CMT)	Lat	Long	Mw	mb	Ms	Mo	Nodal Plane 1 strike	Nodal Plane 1 dip	Nodal Plane 1 rake	Nodal Plane 2 strike	Nodal Plane 2 dip	Nodal Plane 2 rake
	19980825		15	29.86	88.31		5.8			14	46	-67	162	48	-112
	19960703		15	29.77	88.32		5.6			172	45	-102	8	46	-78
	19980828		15	30.08	88.41		5			199	45	-90	19	45	-90
	19980720		15	29.83	88.47		5.7			16	33	-83	187	59	-95
	19980721		15.7	29.93	88.5		5			34	43	-90	214	47	-90
	19981005		33	29.89	88.6		5.2			26	29	-77	191	62	-97
	19960731		15	29.74	88.67		5.4			23	32	-41	150	70	-115
	19790619		24	26.29	87.57		5			179	34	-82	350	57	-95

Thrust

Event Name	Date	Time	Depth (CMT)	Lat	Long	Mw	mb	Ms	Mo	Nodal Plane 1 strike	Nodal Plane 1 dip	Nodal Plane 1 rake	Nodal Plane 2 strike	Nodal Plane 2 dip	Nodal Plane 2 rake
200602030157A	February 3, 2006	1:57:51.7	30.9	26.94	86.70	4.7	5.0	0.0	1.62E+23	279	30	091	098	60	090
200602140055A	February 14, 2006	0:55:28.8	19.2	27.22	88.64	5.3	5.4	4.8	1.12E+24	287	27	126	068	68	073
201310030612A	October 3, 2013	6:12:43.8	27.0	27.17	88.79	4.9	0.0	5.2	2.86E+23	304	37	123	085	59	067
19650112			23	27.4	87.84		5.8			90	75	90	270	15	90

Strike Slip

Event Name	Date	Time	Depth (CMT)	Lat	Long	Mw	mb	Ms	Mo	Nodal Plane 1 strike	Nodal Plane 1 dip	Nodal Plane 1 rake	Nodal Plane 2 strike	Nodal Plane 2 dip	Nodal Plane 2 rake
082088D	August 20, 1988	23:09:15.9	34.7	26.52	86.64	6.8	6.4	6.6	2.31E+26	230	23	002	137	89	113
200503262032A	March 26, 2005	20:32:15.7	69.6	28.08	87.95	4.7	4.9	0.0	1.62E+23	109	62	179	200	89	028
200705201418A	May 20, 2007	14:18:21.6	13.6	27.23	88.56	4.9	5.0	4.4	2.47E+23	204	58	-004	296	86	-148
201109181240A	September 18, 2011	12:40:59.9	46.0	27.44	88.35	6.9	6.6	6.9	2.78E+26	216	72	-012	310	79	-162
19801119			44	27.37	88.77					214	71	12	120	79	161
19911221			70	27.9	88.14					295	85	180	25	89	5

Event Name	Date	Time	Depth (CMT)	Lat	Long	Mw	mb	Ms	Mo	Nodal Plane 1 strike	Nodal Plane 1 dip	Nodal Plane 1 rake	Nodal Plane 2 strike	Nodal Plane 2 dip	Nodal Plane 2 rake
20090606			31.9	30.99	86.43		4.9			218	76	-9	311	81	-166
20100226			84.5	28.41	86.77		5.1			12	69	-16	108	75	-158
19860620			15	30.82	86.77		6			51	78	-4	142	86	-168
19860719			15	30.88	86.88		5.1			51	78	4	320	86	168
19860110			81.4	28.6	87.09		5.1			140	46	-163	38	78	-45

*Data from Area 4:

Normal															
Event Name	Date	Time	Depth (CMT)	Lat	Long	Mw	mb	Ms	Mo	Nodal Plane 1 strike	Nodal Plane 1 dip	Nodal Plane 1 rake	Nodal Plane 2 strike	Nodal Plane 2 dip	Nodal Plane 2 rake
19760914			82	29.81	89.57		5.4			215	52	112	2	43	65
19800222			10	30.69	89.16		6.3			7	39	-84	180	51	-95
19810816			10	30.87	89.79		5.5			139	36	-132	7	64	-64
19890409			15	28.74	89.94		5.1			330	43	-119	187	53	-65
19930118			15	30.34	90.28		5.9			25	48	-57	161	51	-121
19920730			15	29.46	90.3		6.1			10	42	-94	196	49	-86
19870925			15	29.47	90.34		5			201	45	-90	21	45	-90
20081006			12	29.66	90.5		6.3			44	48	-55	178	53	-122
20081006			13.6	29.56	90.53		5.2			173	43	-121	33	54	-64
20101130			19	29.78	90.51		5.3			201	47	-57	337	52	-120
19960609			83	28.71	92.58		5.2			12	23	-117	221	69	-79
20010310			11	27.67	91.86		4.1			235	30	-95	61	60	-87
19930313			42	27.52	92.03		4			25	20	-60	173	73	-100
20040613			40	26.52	92.48		5			80	70	-80	233	22	-115
19880823			42	26.26	92.85		4.1			160	5	-135	25	86	-86

Event Name	Date	Time	Depth (CMT)	Lat	Long	Mw	mb	Ms	Mo	Nodal Plane 1 strike	Nodal Plane 1 dip	Nodal Plane 1 rake	Nodal Plane 2 strike	Nodal Plane 2 dip	Nodal Plane 2 rake
20040530			9	26.25	92.93		4.9			50	30	-130	274	67	-70
20030115			23	25.94	93.11		3.7			120	45	-110	327	48	-71
19930215			24	26.61	93.27		3.6			30	5	-120	240	86	-88
Thrust															
20090921085A	Sep 21, 2009	8:53:10.4	12.0	27.20	91.63	6.1	6.1	6.1	1.9E+25	281	06	094	097	84	090
20091029170A	Oct 29, 2009	17:00:40.2	15.1	27.20	91.62	5.1	5.3	0.0	6.0 E+23	293	07	107	096	83	088
20050601200A	June 1, 2005	20:06:44.7	19.0	28.81	94.72	5.8	6.1	5.7	7.0E+24	209	06	026	093	87	095
19640901	13 22 37.30		33	27.12	92.26		5.5			46	70	91	223	20	87
19641021	23 09 19.00		37	28.04	93.75		5.9			87	85	90	268	5	91
19660926	05 10 56.20		19	27.49	92.61		5.4			73	70	90	253	20	90
19670314	06 58 04.40		12	28.41	94.29		5.7			93	80	90	274	10	91
19670915	10 32 44.20		57	27.42	91.86		5.8			83	60	90	263	30	90
19700219	07 10 01.50		18	27.4	93.96		5.4			77	85	90	258	5	91
19660926	05 10 56.20		12	27.49	92.61					228	25	58	83	69	104
19641021	23 09 19.00		18	28.04	93.75					233	16	51	93	78	100
19640901	13 22 37.30		4	27.12	92.26					267	13	90	87	77	90
19641021			15	28.04	93.76					265	3	90	85	87	90
19700219			10	27.42	93.95					257	5	90	77	85	90
19651209			29	27.4	92.5		ms= 5.1			102	62	92	278	28	86
19690630			44	26.93	92.71					68	50	60	290	48	121
19920222			22	27.05	91.98		4.8			252	5	88	74	85	90
20010320			21	27.17	92.12		3.6			50	80	95	203	11	63
19930312			25	27.44	92.12		3.5			125	85	85	350	7	135
19871015			25	27.32	92.78		4.5			280	5	85	105	85	90

Event Name	Date	Time	Depth (CMT)	Lat	Long	Mw	mb	Ms	Mo	Nodal Plane 1 strike	Nodal Plane 1 dip	Nodal Plane 1 rake	Nodal Plane 2 strike	Nodal Plane 2 dip	Nodal Plane 2 rake
19870913			21	27.25	92.82	4				265	5	115	60	85	88
19680818			29	26.42	90.62	M=5.1				90	60	90	270	30	90
1982				25.65	91.75					26	60	99	188	31	74
1984				25.75	90.85					15	45	43	252	61	126
1984				25.5	91					92	60	90	272	30	90
19680818			29+/-3	26.42	90.62	M=5.1				90	60	90	270	30	90
20030823			14	25.53	90.6	2.5				40	10	130	180	82	84
20030823			5	25.96	90.61	2				330	60	110	114	36	59
19680418			29	26.42	90.62	5.1				90	60	90	270	30	90
19860219			18	25.1	91.13	5.2				92	70	125	208	40	32
20030401			14	25.76	91.59	3.4				5	25	125	147	70	75
20040607			15	25.98	92.24	5				100	50	70	310	44	113
19750603	00 38 54.30		8	26.59	93.91					135	59	85	325	31	99
20040112			34	26.71	92.23	4.1				70	60	110	214	36	59
Strike Slip															
Event Name	Date	Time	Depth (CMT)	Lat	Long	Mw	mb	Ms	Mo	Nodal Plane 1 strike	Nodal Plane 1 dip	Nodal Plane 1 rake	Nodal Plane 2 strike	Nodal Plane 2 dip	Nodal Plane 2 rake
111980A	November 19, 1980	19:00:55.8	44.1	27.42	89.05	6.2	6.0	6.1	2.98E+25	209	51	-002	301	89	-141
032503D	March 25, 2003	18:51:30.7	55.8	26.92	89.82	5.4	4.8	4.8	1.73E+24	040	70	-021	137	71	-159
021795A	February 17, 1995	2:44:32.2	35.0	27.48	92.62	5.4	5.2	5.1	1.83E+24	322	43	-172	223	84	-044
092698B	September 26, 1998	18:27:13.9	33.0	27.87	93.60	5.0	5.4	0.0	3.60E+23	233	26	118	022	67	077
201304160834A	April 16, 2013	8:34:13.0	39.6	28.67	95.12	4.9	5.2	0.0	3.26E+23	300	39	090	120	51	090
19730801			85	29.59	89.17		4.9			220	60	155	323	69	32
19920307			80	29.62	89.19					350	85	-175	260	85	-5

19920404			80	28.15	87.98				46	68	-23	145	69	-156
19890203			15	29.74	90.13	5.4			221	77	-9	313	82	-166
20081008			14.7	29.76	90.57	5.5			69	62	-25	171	68	-150
20060223			12	26.91	91.94	5.4			321	73	-173	229	84	-18
19640218			30	27.4	91.18	5.6			122	50	90	302	40	90
19700219			6	27.4	93.96				38	15	152	79	83	77
19950217			37	27.61	92.34				317	62	167	53	79	29
19640901			33	27.12	92.26				22	64	-14	118	77	-153
19660926			20	27.49	92.61				314	56	41	198	57	138
19670915			19	27.42	91.86				68	64	-153	325	66	-29
19780419			51	27.67	92.68	ms=4.4			56	80	-5	147	85	-170
19830202			42	26.9	92.88				315	72	158	52	69	19
19930312			40	27.34	92.17	3.6			50	40	-170	312	84	-50
19950217			37	27.61	92.34	5			317	62	167	53	79	29
20011123			20	27.35	92.62	3.5			290	50	-160	187	75	-42
19950217			35	27.48	92.62	5.4			322	46	-172	226	84	-44
19921022			19	27.22	92.82	5			10	80	160	104	70	11
19991005			33	25.88	91.89	5.2			244	68	12	149	79	158
19630621			38	25.13	92.09				238	88	-70	333	20	-175
19840922			29	26.49	92.15	ms=5			301	86	33	208	57	175
1984				25.55	90.75				36	72	52	284	41	152
1984				25.85	90.75				42	56	14	304	78	145
1984				25.7	91.15				38	48	13	299	80	137
19630621			38+/-4	25.13	92.09				238	88	70	143	20	175
20031001			24	26.28	90.01	3.2			150	90	40	60	50	180
20030930			26	25.66	90.08	2.1			224	62	-15	321	77	-151
19820705			13	25.91	90.3	5			287	80	-149	191	60	-12

20031003			16	25.75	90.54	2.2			120	10	160	230	87	81
			11	25.77	90.68	2			37	69	159	135	70	22
20010227			17	26.14	90.73	4.3			170	55	30	62	66	141
20040604			12	25.86	90.8	5.3			80	80	-140	342	51	-13
20031002			20	26.13	90.88	2.6			240	70	10	147	81	160
20031112			12	25.65	90.99	1.5			315	60	-30	61	64	-146
20040128			62	25.31	91.08	3.6			340	80	130	82	41	16
19820831			33	25.38	91.5	5			325	72	137	71	50	24
20030929			6	25.62	91.63	1.9			100	80	150	196	61	12
19921022			22	25.46	91.74	4.6			5	15	30	246	83	103
20040120			41	25.56	91.84	3.7			230	40	10	132	84	130
19991005			33	25.88	91.89	5.2			244	68	12	149	79	157
19921029			43	25.31	92.04	5.2			355	70	25	256	67	158
19630621			38	25.13	92.09	5			238	88	-70	333	20	-175
19970508			30	25	92.23	5			239	79	2	149	88	169
19970508			30	25	92.230003	5			239	79	2	149	88	169
19710717			36	26.41	93.15	2.6*E17 Nm			79	60	46	322	51	141
19840321			15	26.76	93.29				326	66	14	230	77	155
20010220			56	26.4	93.22	3.4			125	80	25	30	65	169
19840922			28	26.49	92.15	5.2			59	86	31	327	59	176
20040112			38	26.66	92.29	3.9			270	90	10	360	80	0
20030104			23	25.86	92.58	3.8			222	62	-30	327	64	-149
20010215			44	26.68	92.59	4			60	80	35	323	56	168
20010406			48	26.52	92.76	3.7			0	55	140	116	58	43
19830202			45	26.9	92.87	5.2			39	70	129	152	43	30
19911111			45	26.32	92.88	4.3			5	45	-140	244	63	-53
19910623			27	26.22	93.11	5.2			20	80	15	287	75	170

19710717			36	26.41	93.15		5			79	60	46	322	51	141
20040112			20	26.1	93.28		4.7			20	80	10	288	80	170
19840321			35	26.76	93.3		5			51	80	141	149	52	13
19930227			20	26.48	93.33		3.9			225	70	-25	324	67	#NAME E?

*Data from Area 5:

Strike Slip															
Event Name	Date	Time	Depth (CMT)	Lat	Long	Mw	mb	Ms	Mo	Nodal Plane 1 strike	Nodal Plane 1 dip	Nodal Plane 1 rake	Nodal Plane 2 strike	Nodal Plane 2 dip	Nodal Plane 2 rake
061979B	June 19, 1979	16:27:12.4	24.0	26.28	87.57	5.0	5.1	4.5	3.84E+23	179	34	-082	350	57	-095
021986C	February 19, 1986	17:34:30.3	18.0	24.89	91.18	5.3	5.3	4.9	1.08E+24	340	50	180	070	90	040
100599F	October 5, 1999	17:04:50.8	33.0	25.88	91.89	5.2	5.3	4.5	6.74E+23	244	68	012	176	79	158
032503D	March 25, 2003	18:51:30.7	55.8	26.92	89.82	5.4	4.8	4.8	1.73E+24	040	70	-021	137	71	-159
200602232004A	February 23, 2006	20:04:58.0	12.0	26.91	91.94	5.4	5.5	5.3	1.88E+24	321	73	-173	229	84	-018
201210021837A	October 2, 2012	18:37:39.0	35.5	26.78	92.95	4.9	5.2	0.0	2.52E+23	089	53	044	329	56	134

*All data in these tables were obtained from the ANSS catalogue (USGS), Baruah *et al.* (2014), and the Global Centroid Moment Tensor Project catalogue (GCMT).